PCF-Mach Zehnder Interferometer Sensor employing the splitting of the surface plasmon mode

by

Ahmed Mujtaba Al Naser (170021089)
Fatema Zerin Jaba (170021098)
Fariha Anzum (170021118)

A Thesis Submitted to the Academic Faculty in Partial Fulfillment of the Requirements for the Degree of

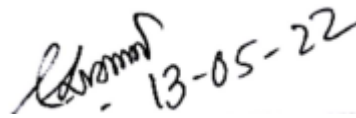**BACHELOR OF SCIENCE IN ELECTRICAL AND ELECTRONIC ENGINEERING**

Department of Electrical and Electronic Engineering
Islamic University of Technology (IUT)
Gazipur, Bangladesh

May 2022

PCF-Mach Zehnder Interferometer Sensor employing the splitting of the surface plasmon mode

Approved by:

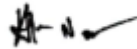
Prof. Dr. Mohammad Rakibul Islam

Supervisor and Head of the Department,
Department of Electrical and Electronic Engineering,
Islamic University of Technology (IUT),
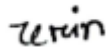Boardbazar, Gazipur-1704.

Date: 13-05-2022

DECLARATION

It is henceforth proclaimed that the authors completed the work displayed in this thesis paper under the supervision of Professor Dr. Mohammad Rakibul Islam, Department of Electrical and Electronic Engineering (EEE), Islamic University of Technology (IUT). It is also claimed that no part of the work was submitted elsewhere in order to obtain a degree. Furthermore, whenever we recommended other people's work, we mentioned specifically the citations.
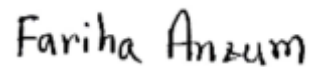
Authors

Ahmed Mujtaba Al Naser
ID: 170021089

Fatema Zerin Jaba
ID: 170021098

Fariha Anzum
ID: 170021118

Date: 13-05-2022

Table of Contents

List of Figures

List of Tables

List of Acronyms

AS	Amplitude Sensitivity
AI	Amplitude Interrogation
CL	Confinement Loss
EMI	Electromagnetic Interference
EML	Effective Material Loss
FBG	Fiber Bragg Grating
FEM	Finite Element Method
ITO	Indium Tin Oxide
LPG	Long Period Grating
MZI	Mach Zehnder Interferometer
NA	Numerical Aperture
PBG	Photonic Band Gap
PCF	Photonic Crystal Fiber
PML	Perfectly Matched Layer
RI	Refractive Index
RW	Resonance Wavelength
RNA	Ribonucleic Acid
RIU	Refractive Index Unit
SP	Surface Plasmon
SPP	Surface Plasmon Polariton
SPW	Surface Plasmon Wave
SPR	Surface Plasmon Resonance
TIR	Total Internal Reflection
THz	Terahertz
TiO$_2$	Titanium dioxide
WS	Wavelength Sensitivity

Acknowledgements

Abstract

In past decades, there have been great interest among researchers to utilize the usage extents of photonic crystal fibers or PCFs, more eminently in sensing purposes. PCFs are compact in nature and can be easily integrated in optical systems. Though many PCF design prototypes are available, an easy fabrication friendly PCF designs are of great need. In our research work, we have implemented three distinct types of sensing mechanisms in photonic crystal fibers; most importantly which can be easily manufactured using current technologies. The designs have been implemented using COMSOL Muliphysics which utilizes the finite element method (FEM). The first type of sensing mechanism involves the launching terahertz wave through PCF cross-section; the Terahertz based sensing. The target analyte are filled inside the core of the PCF sensor and percentage of the output transmitted wave power is measured. In THz based sensing, we have proposed two different types of designs. In the first design, we have analyzed hexagonally defined porous cladding used to detect cyanides; which obtained maximum sensitivity of 99.75%. Next we designed a square structured cross-sectional PCF sensor for sensing of amino acids and the proposed sensor exhibited an optimum relative sensitivity of 99.98%. The second type of sensing mechanism we have analyzed using PCF is Surface Plasmon Resonance (SPR) based sensing. In this design, we have used a combination of gold and titanium dioxide for generating surface plasmon wave, necessary for this sensing mechanism. The sensor presented a remarkably high amplitude sensitivity of 4646.1 RIU^{-1} and wavelength sensitivity of 10000 nm/RIU. Most recently, we have implemented a PCF based Mach Zehnder Interferometer utilizing splitting of surface plasmon mode. The novel sensor evinced an outstanding sensitivity of 14.152 dB/RIU. All the proposed sensor designs have been reviewed in details in the following chapters. It is our hope that the proposed sensor models would have major contributions in analyte sensing in different sectors and industry.

Chapter 1

Introduction

1.1 Background History

Since digital optical equipment is readily accessible, optical biosensors are widely utilized to detect and investigate bio-molecular interactions. The first optical biosensor was promoted in the late 1980s. The primary goal of an optical sensor is light detection, where optical intensity or electromagnetic fields vary owing to the presence of different specimens. Conversion of optical rays into electrical signals is possible with the help of advanced machinery known as an optical sensor, which is capable of converting optical rays into electrical signals that determine the variation and response of ambient conditions or compute the strength of electromagnetic radiation. A few optical sensor methods, like surface plasmon resonance, and evanescent wave absorption spectroscopy, are available for this purpose. However, because to its broad variety of uses and excellent sensitivity, SPR has attracted widespread attention.

Surface Plasmon Resonance-based optical chemical and bio-molecular sensors are among the most sophisticated optical sensing devices [1]. SPR sensors have become an effective optical sensor for bio-molecular experimental evaluation and bio-molecular research in a broad sense due to their capability to analyze and evaluate the interaction between a particle isolated on the sensor surface and its conversing molecular companion in a solution [2]. Surface plasmon resonance optical sensors begin by generating the surface plasmon wave (SPW), which can be accomplished by matching the incident light frequency of the polarization as well as transverse magnetic (TM) surface electrons, causing the free metal surface electron to resonate and propagate along the interface region. SPR sensors need the use of a metallic component that transports a significant quantity of free electrons. These liberated electrons supply the true fraction of the negative permittivity required for plasmonic materials. The traditional prism-based Kretschmann arrangement is extensively employed for SPR-based sensors, in which transverse magnetic light is incidental on a prism covered with plasmonic materials and forms

surface plasmon polaritons waves that propagate along the surface [3]. The propagation constant of the surface plasmon mode changes as the dielectric refractive index changes. This modification impacts the coupling state of the light wave and the SP wave, and the changes may be detected and studied using one of the optical wave characteristics interacting with the SP mode.

SPR-based optical sensors have piqued the interest of researchers due to their distinct and well-established properties; high resilience; small and simple probe design; and increased sensitivity. Because of their advantageous behavior, SPR sensors are now being investigated in a range of areas, such as water quality assessment, food hygiene observation, medical diagnostics, real-time tracking, carbon monoxide detectors, strain sensing, and temperature sensing [2],[4],[5],[6],[7],[8],[9],[10]. The SPR technique also facilitates the implementation of nano-electronic and photonic elements for ultra-compact optical applications [11],[12]. The investigation of SPR-based biosensors began in 1983 when Liedberg et al. launched SPR biosensors in the domains of gas detection and bio-sensing [8] and described the prism-coupling approach. The point cross-examination approach is used by prism-based SPR sensors. Nevertheless, the prism-based sensor is unsuitable for distant sensing since it has several optical and mechanical components, making the sensor large in size. To alleviate these restrictions, investigators have modified the prism with fiber, which has grown in popularity due to promising characteristics such as atypical dispersion, elevated nonlinearity, infinite single-mode behavior, label-free sensing, adjustable increased birefringence and integrity [13],[14]. As a result, PCF-based sensors are well suited for distant sensing. Following extensive study, an upgraded sensor known as a PCF-based SPR sensor was developed. It is highly sensitive and has a smaller resonance peak than conventional fiber-based sensors [15],[16],[17],[18],[19],[20] resulting in greater precision while sensing an unidentified analyte. Furthermore, by varying structural factors such as pitch, bore of air holes, and total number of various shaped rings and air cavities, PCF-based sensors may undoubtedly get a greater command of the transient field.

In our proposed work, we have designed a PCF based Mach Zehnder Interferometer for unknown analyte sensing. Though fiber optic MZI sensors have been presented by many researchers in previous years, the utilization splitting of "metastable" surface plasmon mode into two independent SPP modes have not been implemented in a photonic crystal fiber.

1.2 Problem Statement

Various SPR sensing elements have been reported to date. Because of the coating material of metal layers and fluid penetration within the surface air-hole to manage the propagation of light in a particular way, such sensors initiate elliptical air-slots, as well as many tiny air-holes within the given location, making the configuration of the sensor advanced in terms of manufacturing. As an effective subject of study, various designs for SPR-primarily based optical devices have been developed by researchers, and significant progress has been made. Although internal sensing is more sensitive than exterior sensing, it is more costly and has a more complex structure. So far, the restrictions identified for SPR-based primarily optical sensors include manufacturing issues, a weak evanescent field, a difficult design for high sensitivity, and a significant loss.

Thus, the majority of the suggested sensors' structures were difficult to produce due to a protective film of metal layers and liquid intrusion inside the air-hole surface, and the performance of those sensors was found by following the within sensing. Multiple SPR-based PCF sensors were found concurrently, with the metal and detecting layers positioned outside of the fiber framework to change the sensor layout. Nevertheless, in order to manage the propagation of light in a given direction in order to reinforce the temporary field, these sensors introduced noncircular air-holes as well as many small air-holes squared by selection placed within the specified location, making the sensor framework sophisticated in terms of fabrication operation. On the contrary, attaining great sensitivity with a low loss continues to be a problem for these sensors.

1.3 Research Objective

Initially, optical fiber was primarily employed for transmission. Thus, one of the study challenges was to obtain high birefringence while using the least amount of effective material, confinement loss, dispersion, bending loss, scattering loss, and so on. So far, the lowest EML value achieved is 0.009 [21]. As a result, further lowering the value is difficult and, more significantly, unnecessary due to the complexity of design. The confinement loss and other characteristics are the same. As a result, this subject has been saturated, with virtually little opportunity for future advancement, and researchers are currently focusing less on this area

since SPR is more promising and has more potential for study than transmission applications. The goal of our thesis was to investigate recently published SPR-based designs and conduct a review based on those papers in order to correctly comprehend the SPR phenomenon and its associated terms and to create our own design based on it in order to give a dependable solution to the challenges listed above.

In our future works, we are eager to design more intricate cross-sections for PCF based MZI sensors and discover their usage extents. Other than gold, we want to analyze with different plasmonic materials and implement MZI based PCF sensors for not only analyte detection, but also sensing of different physical parameters as well.

1.4 Motivation

This study is totally supported by simulation work. The COMSOL program is used to audit all coordinated sensors, and their functionality is refined utilizing wavelength interrogation and amplitude interrogation methodologies. Before evaluating the anticipated sensors, the accuracy of the simulation processes is proven using the available literature. The chosen metal coating, liquid infiltration, and internal sensing concerns of the proposed PCF SPR sensors are scrutinized.

Surface plasmon resonance enables the sensitive detection of bio-molecular interactions without the need to label probe molecules with fluorescent markers or use color-changing substrates, which opens up a wide range of applications. It is common practice to conduct DNA and ribonucleic acid experiments by observing the interactions of complementary base pairs in real time. It will detect the presence of viruses in blood samples, similar to an infectious illness, by detecting interactions with virus-specific antigens. It does biology on one side and physics on the other. In addition, biomolecules squarely deployed on the surface of the gold film operate as molecular probes in biology and physics. Infrared emission causes a resonance with surface plasmons inside the film, resulting in a minimum and mirrored optical strength at a certain angle.

SPR technology is often democratized, making it available to everyone in an instrument that is rapid, accurate, and simple to use. It is often used to investigate antibodies, bacteria, viruses, DNA, RNA, mRNA, hemoglobin, hormones, macromolecules, and so on. It may also be employed in physics, physical science, and software packages in the near future. As a result, one will specialize in its biological applications, physics, biology, and education. SPR

technology is one of the most promising analysis spaces at the moment, with a vast field to study and perform analysis in physics, biology, and chemistry.

1.5 Thesis Framework

The thesis book is composed of nine different core chapters. An overview of the following chapters has been given in this section.

Chapter 2: An overview of Photonic Crystal Fiber has been discussed, which includes the types of available PCFs, the advancement of PCFs and their modelling and simulation algorithm.

Chapter 3: Discussion on Surface Plasmon Resonance, comprising of its history, how surface plasmon resonance leads to creation of surface plasmon waves and surface plasmon polaritons. And finally, the advantages of SPR along with its drawbacks.

Chapter 4: Covers the analysis of SPR based PCF sensors, an overview of why it is popular among researchers, different configurations and methods of PCF-SPR sensors and different plasmonic materials used in PCF-SPR sensors and prototypes.

Chapter 5: Comprises the mathematical modelling of the materials that are used in PCF sensors along with formulas used to derive the performance parameters of the proposed sensors.

Chapter 6: Mathematical formulation, simulation results and performance analysis of THz based Square structured PCF sensor, used for human body protein detection.

Chapter 7: Mathematical formulation, simulation and performance analysis of THz based hexagonal outlined PCF sensor used for cyanide sensing.

Chapter 8: Mathematical formulation, simulation and performance analysis of PCF-SPR sensor used for analyte, strain, temperature and magnetic field sensing.

Chapter 9: Comprises our most recent work on PCF-SPR Mach Zehnder Interferometer. The mathematical formulation, splitting phenomena, sensing mechanism, performance analysis has been discussed.

Chapter 2

Overview of Photonic Crystal Fiber

2.1 Introduction

Photonic-crystal fiber is a type of fiber optics that has excellent waveguiding capabilities. It has a stronger capacity to limit light than normal optical fibers. Researchers identified PCF applications such as optical fiber interchanges, laser diodes, non-linear systems, high control distribution, and different gas sensors, data transmission in the THz domain, and so on. Teflon [22], TOPAS[23], and PMMA[24] are all common crystal fibers. TOPAS is recognized as the most ideal material for waveguide propagation due to its exceptional water barrier qualities [25], as well as its excellent biosensing capabilities [26]. Birefringence is one of the critical factors for porous fiber that is useful for polarization-maintaining sensing devices [27].

In this chapter, we provided a brief overview of Photonic Crystal Fiber (PCF), its categorization, the contrast between PCF-based fiber and traditional fiber, and the light-guiding technique of PCF. EML, chromatic dispersion, bending loss, confinement loss, birefringence and effective area are some structural qualities which are discussed. Sensors made from optical fibers, include refractive index sensors, microband fiber optic sensors, and surface enhanced sensors. Raman Scattering and surface plasmon sensors, various sensing techniques, and some simulations are also covered in various sub-sections.

2.2   Brief Description of Photonic Crystal Fibers

2.2.1 Types of PCF

Light-waves are entrapped inside the core area of photonic crystal fibers, resulting in significantly improved wave-guiding capabilities than existing traditional optical fibers. While constructing PCF, the backdrop material employed enhances the fiber's flexibility while also lowering the total production cost. PCF manufacturing is superior than traditional optical fiber

fabrication. PCF is classified based on its architectures, fiber characteristics, and specialized guiding qualities. PCFs are specified into two categories: index-guiding fibers and photonic bandgap fibers.

IG-PCF: There are several types, such as highly nonlinear fibers or HNL fibers, which have small core sides to ensure focused mode encirclement. High numerical aperture fibers, or HNA fibers, have a microstructure protective covering and a hoop of air holes around the cladding, whereas larger mode space fibers, or LMA fibers, have a larger core size and a low index of refraction to confirm a greater effective area. In this case the phenomenon of complete internal reflection traps light waves within the core.

PBG-PCF: These fibers have a low index material core and periodic micro-structured patterns. The RI in the core is lower than in the photonic crystal cladding area. The photonic bandgap technique, which differs from reflected light, guides light waves through into the fiber. Air-Guiding fiber or Hollow Core and LIC fibers or Bragg fibers are two types of Photonic Bandgap Fibers.

2.2.2 Index-Guiding and Photonic Bandgap Fibers

In the case of optical fibers, M-TIR is an acronym for total internal reflection. They rely on a high-index core made of pure silica, surrounded by a micro-structured layer with a low index of refraction. This cladding zone is very wavelength dependant, which is not the case with pure silica, and as a result, photonic crystal fibers differ significantly from typical optical fibers. Since there is an integration of tiny cores and phase-matching conditions that are similar to accessible sources, it is possible to generate an extremely coherent super-continuum utilizing photonic crystal fiber technology. It is now feasible to create optical fibers with large mode-field widths and control over the refractive-index profile, allowing for greater beam-quality fiber guiding and amplification.

It is a separate type of optical fiber having features that varies from M-TIR guiding optical fibers. The generation of photonic band gaps is ensured by the planned micro-structured arrangement in the cladding area of PBG fibers. Light waves of a specific wavelength cannot flow through into the fibers. The core areas of PBG fibers are generated by introducing a flaw

in the structure of the fiber, resulting in a region in which light may readily propagate. Because the faulty region generates a low index-guiding core, light can only travel through it readily.

2.2.3 Hollow-Core and Solid-Core Fibers

One of the particular kinds of photonic band gap fibers is hollow-core fiber. The electromagnetic field is contained within an air-filled core in this case. However, unlike other photonic band gap fibers, light is only steered in a narrow spectrum by air-core fibers. For fibers guiding about 1550 nm, the usual bandwidth is 200 nm. The anti-guiding core area is underneath this region [28]. Other favourable features of hollow-core fibers are not often present in other conventional fibers. Because the material inside the core contributes relatively little in this case, the overall distribution of photonic bandgap fibers remains larger where wave-guide scattering predominates.

Solid-core photonic bandgap guiding fibers are another essential form of photonic bandgap guiding fiber. The magnetic wave is restricted within the same solid-core in this type of fiber, and there are arrays of high-index areas implanted inside the material silica in the cladding sections. These fibers can only direct light waves through a small portion of the spectrum. This mixture of doping concentration photonic bandgap fiber and specifically dispersive properties provides the laser community with a wide variety of options.

2.2.4 Light-guiding Mechanism of PCF

In 1996, the first experiment of light guiding in a PCF was performed within a solid-core fiber. A rod was utilized to replace the center air capillary in an air capillary network [28],[29]. PCF's light-guiding technology is divided into two types: Total Internal Reflection (TIR) and Photonic Bandgap (PBG). Total Internal Reflection (TIR) is the most fundamental and quite well light-guiding property in conventional fibers. The majority of TIR crystal fibers have a solid core encircled by a coating with a simple periodic pattern of air slots [30]. Photonic crystal fibres (PCFs) are a type of optical fiber distinguished by a standard pattern of micro-capillaries that constitute the cladding of the fiber around a solid or cylindrical imperfection core [31].

Photonic Bandgap PCF or Hollow Core PCF is the name given to light that is guided using a PBG mechanism. The lack of a single air-hole in the framework, and also a doped core with a high index score, distinguish IG-PCFs. PGB-PCFs have a hollow heart. Generally, increasing the air hole creates a hollow core in the centre of the construction. PCFs can outperform their conventional equivalents in a variety of applications, including huge endlessly single-mode fibers, dispersion correction, single-polarization and high birefringence guiding, and nonlinear implementations.

2.3 Evolution of PCF

Fibers having a periodic transverse microstructure are measured using Photonic Crystal Fibers. It was originally studied at the University of Bath in the United Kingdom in 1996. Philip Russell originally presented in a silica fiber a hexagonal lattice of air slots, having a solid in 1996 or hollow in 1998, light guiding core at the center. It took four years of technical research for the original demonstration, and since then, fabrication processes have advanced to the point that creating the microstructure in air-glass PCF to precision of 10 nm on dimensions of 1 µm is now feasible.

2.4 Methodology and Simulation

2.4.1 Different Methods

A significant amount of numerical method has already been completed for the PCFs simulation. There are several numerical approaches for investigating the characteristics of PCFs. The Fresnel equation indicates the phenomena of light reflection at a single contact between two media. When there are many contacts, reflections are partially transmitted and then partially reflected. A layer structure's total reflection is the sum of an unlimited number of reflections. According to Maxwell's equations, the electric field has simple continuity requirements across borders from one medium to another. The plane wave approach is extremely useful for determining modal solutions to Maxwell's equation. In calculating over a periodic geometry, the plane wave approach is utilized. It is a vectoral approach that is directly applied to the design of fibers. The measurement of confinement loss is one of the most important of all PCF parameters. PCFs are used in light-related applications. If the loss is

considerable, the releasing light will shortly fade away. As a result, it will be impossible to pass through into the fiber and so be unsuitable in any of the purposes. The plane wave expansion method, eigenmode expansion technique (EME), multipole method (MM), and finite element approach are all well-known methods for solving modes (FEM).

2.4.2 Finite Element Method

In engineering and mathematical fields, the finite element method is a conventional numerical process for solving differential equations. Heat transmission, fluid movement, electromagnetic potential, and mass motion are common problem areas of concern. FEM is an arithmetic approach for pre-guessing solutions to partial differential equation boundary value problems. In this strategy, finite elements are employed to subdivide the whole issue domain. FEM is the sum of divergence material characteristics and a simple presentation of the entire solution. FEM is more suited to solving complicated nonlinear situations [32]. The fundamental advantage of FEM is that it can handle both complicated 2D and 3D domains [33]. When the issue requires local mesh improvement, FEM produces excellent results. Because the suggested model requires mesh refinement, FEM is used. The FEM solves non - homogeneous domains better than homogeneous domains, which is a benefit. One of the primary motivations for using FEM is its capacity to simulate compositionally and mathematically complicated issues [34].

2.4.3 Effective Refractive Index and PML

Perfectly Matched Layers are extra areas or domains that absorb input radiation rather than reflecting it (PML). It is a component of the model and will be composed of various absorbent materials of varying thicknesses. It is necessary to have isotropic permeability and permittivity with the physical medium outside the PML in order to avoid reflections. We may utilize Maxwell's equation to define the PML by applying a complex valued coordinate transform under the extra constraint.

2.5 Conclusion

In this chapter, the principles of photonic crystal fiber were covered first, followed by guiding mechanisms. It was difficult to include every paper, patent, or detail of each sensor since photonic crystal fiber sensing is a continuously expanding area. Nonetheless, an overview of photonic crystal fiber-based sensing was provided, along with the possibilities offered by these fibers, indicating their relevance in optical sensing technology. The range of unusual features of photonic crystal fibers provides the opportunity for new and improved sensors beyond what ordinary fibers can deliver.

Chapter 3

Surface Plasmon Resonance

3.1 Introduction

Surface Plasmon resonance is a label-free, optical detecting method used to monitor the periodic interactions of many molecules. SPR is a physical process that occurs when light strikes a metal sheet under total internal reflection circumstances and causes resonant oscillations of conductivity electrons at the interface between negative and positive permittivity material. SPR monitors the binding interactions between a molecule on the device surface and its binding partners in high resolution over time. When the molecules join, the index of refraction at the surface changes, causing a shift in the angle of the lowest reflected intensity. SPR-based biosensors will be effective instruments for capturing molecular interactions. The combination of three individual pieces- the detector, the device surface, and the sampling delivery mechanism- is critical to the experiment's completion.

3.2 History

Late in the 1960s, Kretschmann [35] and Otto [36] revealed the optical phenomena of surface plasmons through attenuated total reflection. Surface plasma waves are stimulated optically in two ways: suppressed total reflection in prism coupler-based systems and diffraction at diffraction gratings. Nylander and Liedberg [8] were the first to use surface plasma waves for sensing. This approach has been frequently used for the characterization of thin films [37] and biochemical sensing [38],[39] due to its relative simplicity.

In the 1980s, SPR and similar methods were used to probe films as well as biological and chemical reactions [37] .These approaches enable the user to explore the association between fixed sensors and analytes in solution instantaneously, even without the sample having been labeled. There are several approaches to offer suggestions on the selectivity, kinetics, and sensitivity of the contact, as well as the analyte concentration, by measuring binding rates and levels. One of the researchers, Pharmacia, became interested in the SPR sensor in the early

1980s and began to investigate it. In 1984, Pharmacia established "Pharmacia Biosensor AB" to develop, construct, and sell a practical SPR-machine [40]; and the development of a silicone microfluidic cartridge has moved the user-friendly SPR-machine closer to reality [41].

It is unsuitable for distant sensing applications that need a variety of optical and moveable components due to its huge size. A little fluctuation in an analyte's RI may detect the big peak wavelength shift. The wide peak wavelength shift causes a very modest change in the analyte's RI. High sensitivity leads to greater accuracy when identifying an unknown analyte [42]. Plasmonic (sensing) substances are critical to the effectiveness of SPR sensors. It serves as a sensor material for the whole surface plasmon resonance phenomena. It directs incoming light from the cladding section to the metal-dielectric surface, resulting in the surface plasmon wave and surface plasmon polariton. Silver, copper, gold (Au), and other plasmonic materials are used in the SPR sensor. Each one has distinct qualities. Silver (Ag) has a strong resonance peak and is less chemically stable and optically dampening. However, it has an oxidization issue in an aqueous environment, which causes certain limitations when used in a larger sensing approach. A thin coating of graphene may be used as a safer option in this case, but it is very difficult to create and has relatively high prices. It will also be tough to manufacture more. Gold is also chemically stable, which means it does not oxidize quickly in water. It also has excellent sensing performance in all environments [3]. Many studies are being conducted to improve the sensing capability of SPR biosensors.

3.3 Working Principle

Light is focused onto a metallic surface through a glass crystal, and the ensuing reflection is identified at a certain angle of propagating light, generating a faint line within the reflected light that contains a great deal of data. A change in the reflectivity bend indicates an atomic event occurring on or around the metal plate, or a conformational change within the atoms bonded to the film. Analysts may conceive of atomic official events and official energy without the hassle of a label by examining this movement vs. time.
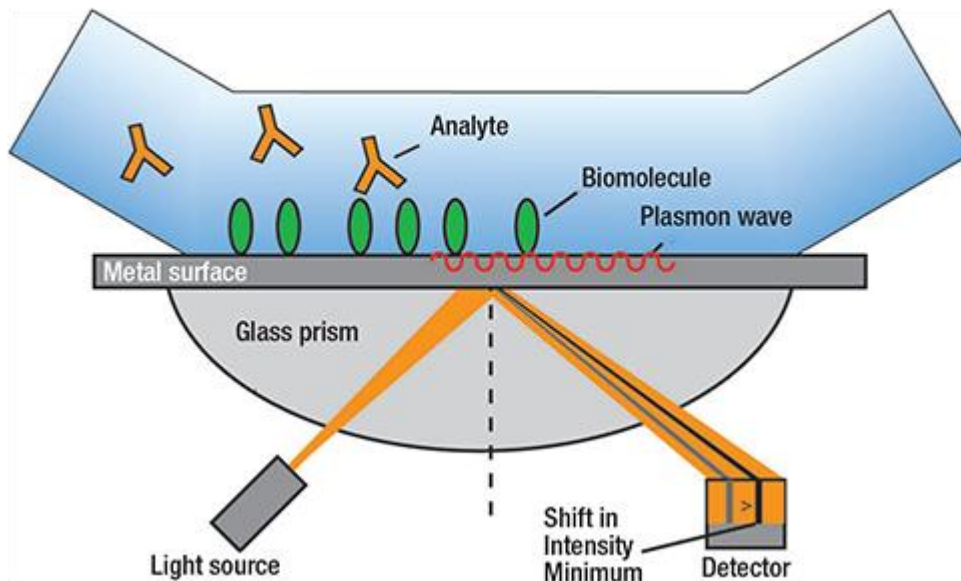
Figure 3.1: A prism on a metal film reflects light, and the reflected beam is recorded and evaluated

3.4 Literature Analysis

Surface plasmon wave (SPW), surface plasmon polariton (SPP), evanescent field, and other plasmonic terminology are associated with SPR sensors. Everything will be explained in the next section.

3.4.1 Surface Plasmon Wave

We've previously been acquainted with the SPR biosensor. A thin metal layer is placed on glass in the SPR biosensor, and a sensor chip is put between the surface and the aqueous compartment. Gold was selected for its chemical stability as well as having large resonance peak shifts. When light propagates through the substrate, its frequency matches the oscillation caused by free electrons at the metal-dielectric contact. Furthermore, it produces the surface plasmon wave. Because the refractive index may be changed, this SPW is highly sensitive.
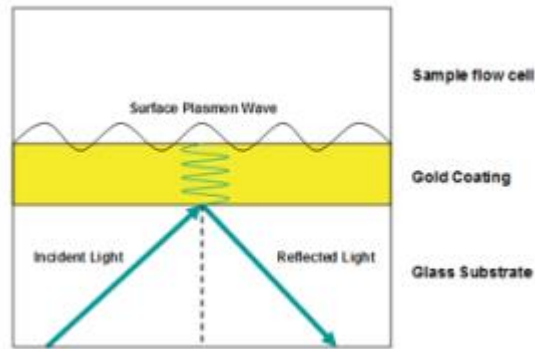
Figure 3.2: Generation of Surface Plasmon Wave

The incident light angle required to support this surface plasmon wave is particularly sensitive to variations in the refractive indices at the surface, as well as the thickness of the sample layer and gold. These are the modifications necessary to monitor the attachment and decoupling of biomolecules. The basic foundation of surface plasmon resonance is this surface plasmon wave.

3.4.2 Surface Plasmon Polariton

It is the movement of electromagnetic oscillations in a metal and dielectric medium junction. The method is analogous to how light is controlled by an optical cable. Incoming light (photons) has a shorter wavelength than SPPs. As a result, SPPs may have more restricted spatial confinement and greater local field intensity. The SPP persists along the contact until the energy is released in either metal concentrations or other forms (such as empty space) [43]. This mode may agitate not only electrons but also photons. Electrons are excited by shooting electrons into the bulk of the metal. Energy is delivered into the main plasma when electrons spread. The frequency and velocity must be comparable in order to ignite a photon.
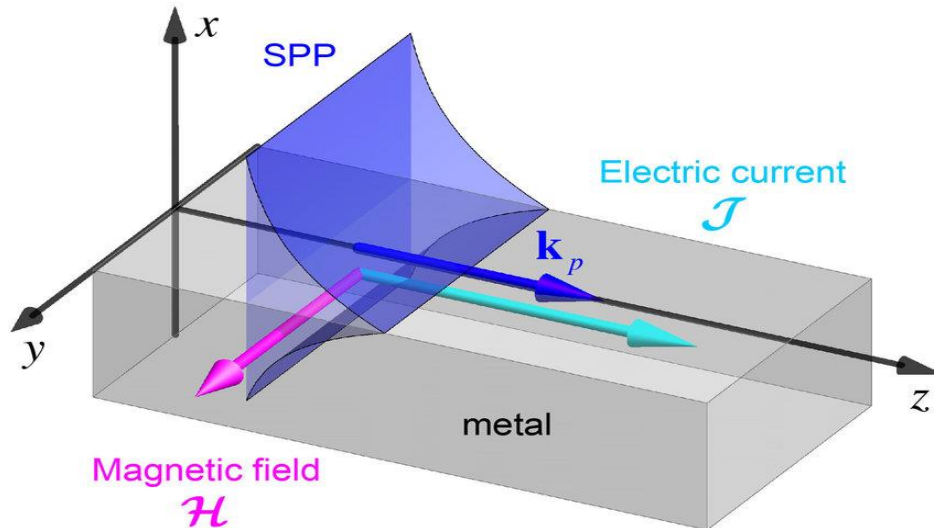
Figure 3.3: Schematic diagram of a Surface Plasmon Polariton (SPP) propagating

Nevertheless, since their dispersion relations vary, a free space photon has little more momentum than an SPP at a given frequency. Due to the absence of momentum, a free-space photon from the air cannot link directly to an SPP.

3.4.3 Evanescent Field

When light is reflected at angles close to the critical angle, a large percentage of the power is transferred to the cladding or medium that surrounds the core. The evanescent wave is a phenomenon that lasts just a short distance from the interface, with power decreasing exponentially with distance. The evanescent field has been used to investigate surface-specific recognition events in real time [44]. Although complete internal reflection is often used in fiber optics to guide light energy down the fiber, a part of the internally reflected wave extends a limited distance beyond the core boundary into the optical cladding (fig. 3.4).
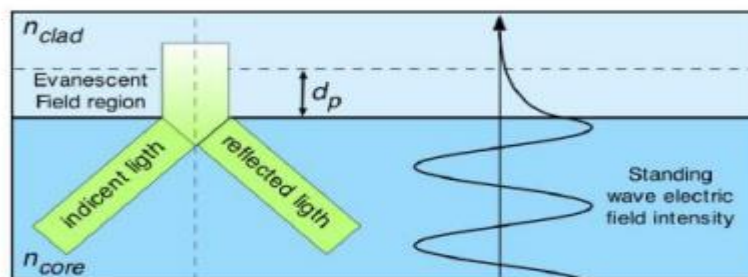
Figure 3.4: Evanescent Wave in Optical Fiber

This is the evanescent wave property, which may be used by removing the fiber cladding and allowing the evanescent wave to expand beyond the core boundary into the surrounding substances. The high evanescent electric field in a system with an absorbing dielectric medium enhances the medium's absorption.

3.5 Advantages of SPR

SPR technology allows monitoring limited activity on a sub-atomic level to be simpler and more precise than at any other time in recent memory, despite the availability of a variety of bio-detecting equipment. Here are some of the most important advantages of employing surface plasmon resonance:

Small sample sizes: SPR requires an insignificant test measure to undertake experiments. Researchers and certain medical practitioners might be able to save money by using less costly materials, making surface plasmon reverberation more accessible.

Sensor chips that can be reused: The ability to recycle sensor chips is another clever feature of SPR. Sensor chips have a direct impact on the data and are an important part of bio-detection. With so much riding on the efficiency and execution of the sensor chip, it's becoming more crucial to realize that these chips may be reused.

Adaptability to complicated samples: Even if only rough samples are available for investigation, surface Plasmon reverberation may be exploited. SPR has been used in a variety of scientific contexts, including serum analysis, to evaluate studies.

Real-time Monitoring: Using SPR technology, researchers may examine how different biomolecules interact over time in a straightforward and relatively low-cost way. It has a wide range of applications in the medicinal and therapeutic disciplines, as well as in the domains of inherited attributes and electricity.

3.6 Drawbacks

SPR biosensor technology has a number of drawbacks as well. Unlike other analytical methods such as mass spectrometry or UV spectrometry, which may be used to analyze the material regardless of whether it is correctly folded and active or not, biosensors need the molecule to be active in order to create a signal. Another disadvantage is that, although

biosensor equipment is generally simple to use, planning and performing an experiment requires some biochemistry knowledge.

3.7 Conclusion

This chapter has covered the optical aspects of planar SPR technology. The physical SPR phenomenon is used in other commercial electronics. It provides a one-of-a-kind sensor concept for label-free biomolecular interactions that combines multiplexing with very high sensitivity. Other essential aspects such as evanescent field penetration depth and surface plasmon propagation length have been addressed for planar SPR devices. Reflectivity or angle shift mode is frequently used to assess SPR-dip shifts. Due to its inherent inertness, gold remains the gold standard for generating surface plasmon resonance events in all commercial equipment. Both commercial and advanced SPR devices exploit these core fundamentals.

Chapter 4

Analysis of SPR based Photonic Crystal Fiber Sensors

4.1 Overview

PCF-based sensors have higher sensitivity and lower resonance peaks than other fiber-based sensors, which means they can detect an unknown analyte with greater precision. Furthermore, by adjusting structural factors such as pitch, the bore of the air holes, and the total count of various shaped rings and air cavities, PCF-based sensors may undoubtedly deserve a greater authority on the transient field. For achieving acceptable sensing qualities, SPR is the chosen approach. When SPR-based technology is combined with a benign characteristic, the desired SPR-based PCF sensors emerge.

SPR is used in this kind of sensor, and it works when light travels through the fiber. As a result, the generated evanescent field falls on the plasmonic metal surface, causing the free electrons to oscillate. As a result, the SPW becomes energized and circulates throughout the core-cladding area. The SPP mode conjoins with the core mode at a certain wavelength to provide phase-matching between the two modes with an equally effective portion of effective RI. In this scenario, a sharper resonance peak is produced at that wavelength, and this peak is significantly dependent on analyte RI. As a consequence, every little change in RI causes the resonance wavelength (RW) to move to a higher or lower wavelength. The variation of the RW for differing analyte RIs may therefore be used to identify an anonymous analyte.

Prism-based and D-shaped sensors are the first steps of SPR-based sensors. PCF sensors were developed after several successful studies. It has gone through a lengthy period of evolution. The plasmonic metal layer and the analyte channel through which the material to be diagnosed passes are either retained outside or within the fiber in current PCF-SPR sensors, depending on the kind of sensor. The following sections provide a brief history, variation, and division of PCF sensors based on the SPR method.

4.2 Design Structure and Performance of PCF-SPR sensors

The surface plasmonic substance (gold, silver, bimetallic, etc.) is used to classify SPR sensors. In a PCF, the plasmonic metal layer may be applied either inside or outside the fiber surface. The geometrical characteristics of PCF have a significant impact on SPR sensor performance. For a straightforward interaction between the metal layer and the evanescent field, design parameters should be carefully determined. When there is a tight link between core-guided mode and SPP mode, sensitivity increases. We can achieve maximal wavelength and amplitude sensitivity by adjusting several geometrical parameters of PCF based on surface plasmon resonance.

4.3 Internal and External Sensing based Sensor

To manage the difficulties of prism-based sensors, the internal sensing type sensor was designed. Internal sensing is a traditional method of sensing in which metal films are placed on the air holes and the analytes are packed inside the hole [45]. The first kind is difficult to execute in practice because coating the interior fiber pores with metal sheets and filling them with analytes is tough. Because of the tiny size of the perforations, these issues occur. Furthermore, keeping the holes' equal thickness throughout manufacture is impossible. Another issue is that the fiber must be measured, emptied, and refilled, all of which takes time. Furthermore, repeated filling and emptying might degrade the sensor's detecting capabilities.

External sensing has become the favored approach for analyte detection owing to superior sensing properties and an advantage in the manufacturing process [46],[47], due to the constraints of internal sensing and D-shaped PCF. It offers services such as sensor cleaning and reuse. Unlike internal sensing, where the metal coating is put within the air holes, there are no pre-steps before sampling since the metal coating is placed outside the fiber. The sensor simply attaches to the analyte solution and displays the required sensor performance within a few minutes.

4.4 Prism based Sensor

Prism couplers are simple, adaptable, and do not need complicated optical apparatus to couple light to SPs. As a result, SPR sensors with ATR methods and prism couplers have become the most popular. In prism-based SPR sensors, all main forms of modulation have been implemented. In SPR sensors based on spectroscopy of SPs, the angular or wavelength spectrum of the optical wave connected to the SP is determined. At a given wavelength and angle of incidence, changes in the intensity or phase of the reflected wave may be monitored. While spectroscopic SPR sensors often have better resolution, they have a lower number of sensing channels. On the other hand, SPR imaging systems may use intensity or phase modulations to make independent measurements in hundreds of sensing channels at the same time. Several prism-based SPR sensor setups have been researched and tested in the lab over time [48]. Many SPR sensing systems have been commercialized as a consequence of successful deployment. However, the prism-based SPR sensor system is sometimes highly expensive and large in size. Though prism-based commercial sensors are available, we concentrated our inquiry on the waveguide-based SPR sensing system due to the shortcomings of prism-based SPR sensing systems. As a result, a detailed examination of the historical evolution of prism-based SPR sensing systems is outside the scope of this thesis and will not be covered here.

4.5 Plasmonic Material Silver based Sensor

The plasmonic substance utilized in the sensor has a significant impact on the sensing performance. Silver has a stronger resonance peak, which results in better FOM output. Figure 4.1 [49] depicts various silver-based sensors. Silver is one of the most conductive metals, yet it oxidizes quickly in wet environments. This effect degrades sensor performance and diminishes sensing accuracy. It has poor sensing performance due to the chemical instability of silver (Ag) and other constraints [50].
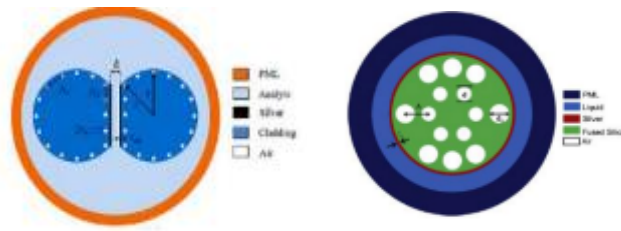
Figure 4.1: Cross-sectional view of different silver-based sensors

4.6 Plasmonic Material Gold based Sensor

This section analyzes several types of SPR designs, their properties, and compares them using gold as the metallic layer, based on the reported design. Silver has a stronger resonant peak than gold, although it is chemically unstable.
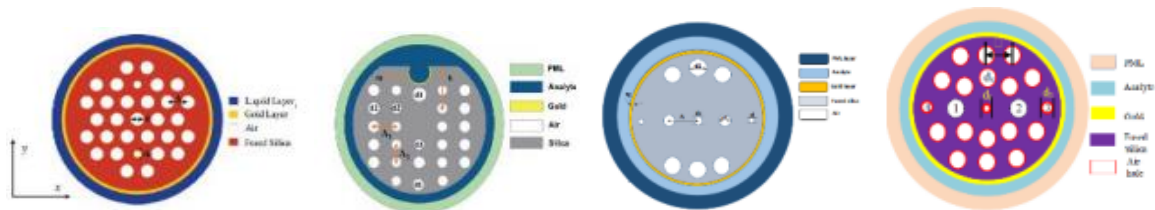
Figure 4.2: Cross-sectional view of various gold-based sensors

Thus, gold has lately become popular owing to its chemical stability and a large change in resonance frequency, resulting in appropriate analyte detection [51].Several studies have been conducted on gold-based biosensors. Figure 4.2 shows sensors of different geometrical structures using gold as the plasmonic material [52].PCF SPR Sensors based on Bimetallic Materials

Many researchers employed a bimetallic layer instead of a single gold layer outside the cladding surface to improve the evanescent field, and under certain situations, they achieved better results than utilizing just gold as the metal layer, which is briefly discussed in this section. Han Liang and Tao Shen suggested a D-shaped PCF Sensor-based SPR using silver as the plasmonic material in December 2020 [Fig 4.3(a)]. The sensor's performance was evaluated by sequentially coating the sensor with grapheme and zinc oxide layers. The polished surface is covered with a substance that simplifies sensor manufacture while also achieving the sensor's goals of reinforcing materials throughout the hole and coating on the hole wall [53].

Ahmmed A. Rifat and G. Amouzad Mahdiraji proposed a PCF SPR sensor in 2015, which utilized silver as the plasmonic material. The coating was made of graphene to avoid oxidation. Placing liquid-filled cores near a metallic channel produces surface plasmon waves. Two comparable cores were packed with high RI liquid to construct a straight line with a central metal channel in this design. On top of a thin silver coating, a graphene sheet covers the inner surface of the fiber's core structure[54].

(a)   **(b)**   **(c)**
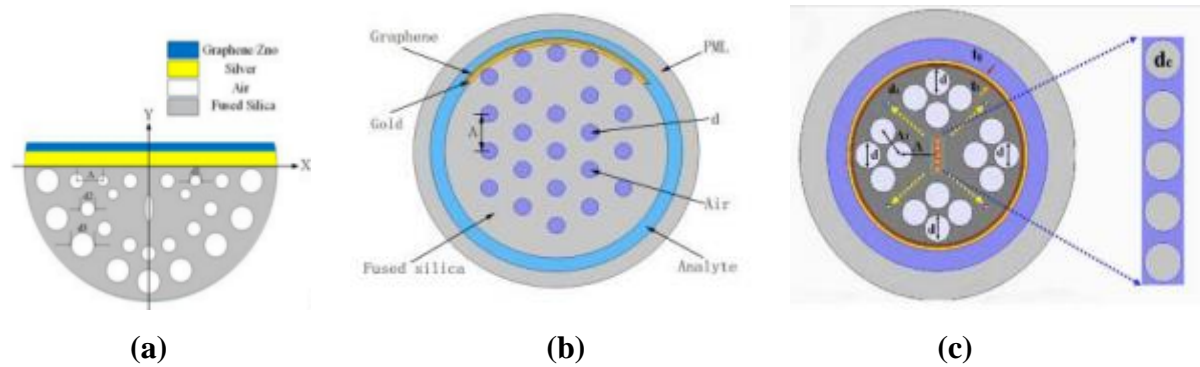
Figure 4.3: Cross-section of discussed PCF SPR sensors based on Bimetallic Materials

Junbo Lou suggested a PCF SPR sensor with gold and graphene bimetallic layers in 2019 [Fig 4.3(b)]. The air-holes in the cladding zone were positioned hexagonally in this design. The fiber core was elevated to form a hexagonal shape with an eccentric core. After adding graphene, the average sensitivity increased from 2938.86 to 5171.51nm/RIU, with the highest sensitivity reaching 8600 nm/RIU [55].

To alleviate gold adhesion concerns, a thin TiO2 coating with improved RI, non-toxicity, and environmental stability is usually utilized between Au and glass [Fig 4.3(c)]. In June 2019, Saiful Islam et al. presented a study describing a tiny, simple, and highly SPR-PCF biosensor. The gold layer had a thickness of 30nm, and a coating of titanium dioxide (Ti) was chosen to inhibit gold adherence. A maximum wavelength sensitivity of 25,000 nm/RIU and a maximum amplitude sensitivity of 1,411 RIU1 were observed using this recommended sensor [56].

4.7 ITO based Sensor

The plasmonic resonance of indium tin oxide (ITO) may be altered by changing the number of metal atoms and oxygen concentration in the material. In 2014, Jitendra Narayan Dash and Rajan Jha developed an SPR sensor based on conducting metal oxide (ITO) that steered surface plasmon waves at the dielectric-ITO interface [57].
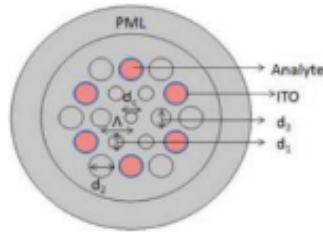
Figure 4.4: Cross-section of discussed PCF SPR sensors based on Bimetallic Materials

The peak resonant frequency of ITO could be tuned by varying its thickness, but unlike other plasmonic materials, there were no band-to-band transitions in ITO. Furthermore, ITO is less expensive than gold and silver, making it more cost-effective. Figure 4.4 [57] shows a sensor that uses ITO as the plasmonic material.

4.8 Conclusion

Researchers experimented with alternative sensor architectures to increase PCF SPR sensors' sensing capability. Their goals were to achieve maximal sensitivity, minimum confinement loss, and practical implementation practicality. By studying the publications, we learned which sort of structure has the highest sensitivity and which plasmonic material may be employed to increase sensing performance. Outside, the precisely matched layer is employed to prevent light from leaving the fiber. Because of its very low temperature sensitivity, fused silica is employed. The externally sensing technique has superior amplitude and wavelength sensitivity than the internally sensing approach. The circular lattice structure has greater sensing capability than the hexagonal lattice structure because light is restricted more in this situation. The D-shaped lattice improves sensing performance, but putting it into practice is difficult. Smaller air-holes allow more light to enter through to the core. When bigger air holes are employed, energy is transferred from the core to the SPP mode. The amount of light that leaks from the core to the cladding is determined by the pitch. As a result, it should

be maintained low. The plasmonic materials are gold and silver. Gold is often selected over silver due to its chemical stability. The addition of another material, such as TiO2, graphene, to plasmonic material improves the sensor's sensing capability.

Chapter 5

Description of Materials and Performance Parameters

5.1 Introduction

This chapter discussed the different materials used in the design of SPR-based PCF sensors. Many materials are used, including silica (SiO2), titanium dioxide (TiO2) and gold (Au). This paper presents the equations that may be used to describe these materials in simulation systems. It's worth noting that just the refractive index (RI) of these materials matters. We've just supplied the RI equations for these materials so far. Because the square-root of permittivity equals the RI, we've provided permittivity equations in certain cases. In this chapter, we looked at the factors that determine sensor performance. These features include things like CL, AS, WS, resolution, figure of merit (FOM), sensor length, and more. The equations that may be used to calculate these parameters are shown and explained in this chapter.

5.2 Material Characterization

This section covers the material characterization equations. We've just finished talking about the materials we used in the research assignments in chapters 6, 7, 8, and 9. It's worth mentioning that the effective RI of certain materials is more difficult. The effective RI of any material may be stated in the complex form $n_{eff} = n + jk$, where n and k represent the real and complex components of the RI, respectively.

5.2.1 Silica (SiO2)

SPR sensors are typically manufactured by laminating plasmonic metal onto the surface of a PCF. The PCF may be made out of glass or polymers. The material of choice for the PCF background is fused silica, also known as silicon di-oxide. In the majority of

situations, undoped silica is used. The RI property of fused silica is calculated using the Sellmeier equation [6]:

$$n_{si}(\lambda) = \sqrt{1 + \frac{B_1 \lambda^2}{\lambda^2 - C_1} + \frac{B_2 \lambda^2}{\lambda^2 - C_2} + \frac{B_3 \lambda^2}{\lambda^2 - C_3}}$$

The Sellmeier constants and the wavelength of light give the value of n_{si}, which is the RI of silica. The Sellmeier constants are shown in Table 5.1. This method may be used to compute the silica RI [58] at a constant temperature of 25 °C. Figure 5.1 depicts the RI of silica as a function of wavelength. On the Celsius scale, the temperature-dependent mineral silica is designated by T. RI n_{si} may alternatively be calculated using the modified Sellmeier equation [9]:

$$n_{si}^2(\lambda, T) = (1.31552 + 6.90754 \times 10^{-6} T) + \frac{(0.788404 + 23.5835 \times 10^{-6} T)\lambda^2}{\lambda^2 - (0.0110199 + 0.584758 \times 10^{-6} T)}$$
$$+ \frac{(0.91316 + 0.548368 \times 10^{-6} T)\lambda^2}{\lambda^2 - 100}$$

The silica RI is calculated using the above two formulas when the applied strain is zero.

5.2.2 Gold

Atomic number 79 is assigned to gold. It is represented by the letter 'Au' and has a relative atomic mass of 196.96657. The melting point of gold is 1064 degrees Celsius. Our SPR sensors have a gold lamination on the outside. It is commonly used as a plasmonic material because of its better behavior than other plasmonic materials. The dielectric constant of gold may be calculated using the Drude-Lorentz model, as illustrated below [59]:

27

$$\varepsilon_{Au} = \varepsilon_\infty - \frac{\omega_D^2}{\omega(\omega + j\gamma_D)} - \frac{\Delta\varepsilon.\Omega_L^2}{(\omega^2 - \Omega_L^2) + j\Gamma_L\omega}$$

The gold permittivity is denoted by the letter ε_{Au}, whereas the high-frequency permittivity, ε_∞ is denoted by the number 5.9673. ω is the plasma frequency, while Γ_D and ω_D are the plasma and damping frequencies, respectively. As stated in equation 5.3, the dielectric constant of gold is a complex number equal to the squared value of gold RI. As a consequence, the gold RI may be computed by square-rooting the dielectric constant, which is another difficult quantity.

5.2.3 Titanium di-oxide (TiO2)

Between the gold and the fiber, a thin layer of titanium dioxide has recently acquired favor. Because the gold layer rapidly flakes off when mild pressure is applied, the TiO2 coating is coated to increase gold adhesion to the fiber. TiO2 is a transition metal that has a high refractive index[60]. As a consequence, it helps to draw ephemeral fields from the core. The wavelength (in Angstroms) and refractive index of the metallic layer TiO2 may be computed using the equation [61] ,where λ and n_t are the wavelength and RI of TiO2, respectively.

$$n_t(\lambda) = \sqrt{5.913 + \frac{2.441 \times 10^7}{\lambda^2 - 0.803 \times 10^7}}$$

5.2.4 Ethanol (C2H5OH)

Hydrocarbons include ethanol. The chemical formula for ethanol is C_2H_5OH. The functional group of ethanol is hydroxyl (-OH). As a consequence, it is classified as an alcoholic beverage. The refractive index of ethanol is a real number that fluctuates with temperature. Ethanol may be used to monitor temperature because of its temperature sensitivity. An SPR-based PCF sensor may be utilized as a temperature sensor when the analyte includes ethanol. As a consequence, we need to know the temperature-dependent RI of ethanol, which is expressed as [9] :

$$n_1 = n_0 + \frac{dn}{dt}(T_1 - T_0)$$

where n_1 and n_0 are the refractive index at T_1 and T_0, correspondingly. At a temperature of 20 degrees Celsius, ethanol has a RI of $n_0 = 1.361$.

5.3 Mathematical Formulation of Parameters

This section has gone through many performance measures that are used to assess sensor performance. Among them are the following: CL, AS, WS, resolution, FOM, and others.

5.3.1 Confinement Loss

Because all other parameters must be measured, CL is the most significant performance statistic for evaluating sensor performance. The CL denotes the amount of energy that has been moved from the core to SPP mode. A portion of the light energy supplied via the PCF sensor's core seeps out and reaches the metal layer region. The quantity of this leaked energy is known as the "confinement loss" (CL). Equations may be used to compute the CL[56]:

$$\alpha\left[dB / cm\right] = 8.686 \times k_0 \times \mathrm{Im}(n_{eff}) \times 10^4$$

The imaginary component of the effective RI, n_{eff} is denoted by Im, whereas the wavelength is represented by $k_0 = 2\pi/\lambda$

5.3.2 Wavelength Sensitivity

Another method of evaluating the sensor's performance is wavelength interrogation (spectral-based measurement), which takes into account the change in resonance wavelength. The following formula is used to calculate a sensor's sensitivity in the WI method [56]:

$$S_\lambda\left[nm / RIU\right] = \frac{\Delta\lambda_{peak}}{\Delta n_a}$$

The difference between two neighboring analytes, RI and the contrast in their associated resonant wavelengths are denoted by n_a and peak, respectively.

5.3.3 Amplitude Sensitivity

Two approaches for assessing sensor potential are the amplitude interrogation technique (AI) and the wavelength interrogation method (WI). A technique for identifying unknown analytes is amplitude interrogation (intensity-based measurement).

The formula [62] may be used to compute a sensor's amplitude sensitivity (AS), where $\alpha(\lambda, n_a)$ is the confinement loss at a specific analyte RI and $\partial \alpha(\lambda, n_a)$ is the confinement loss difference due to two surrounding analyte RIs.

$$S_A \left[RIU^{-1} \right] = -\frac{1}{\alpha(\lambda, n_a)} \cdot \frac{\partial \alpha(\lambda, n_a)}{\partial n_a}$$

The AI method uses a constant wavelength to measure AS, making it straightforward to utilize in practice. Because no spectral adjustment is necessary.

5.3.4 Sensor Resolution

The resolution of a sensor is a feature that helps determine its detection capabilities. The resolution refers to how well even the smallest change in RI may be recognized. If the lowest spectral resolution is $\partial \lambda_{\min}$ and the RW shift is $\partial \lambda_{peak}$, the following formula enumerates the resolutions [56]:

$$R_\lambda \left[RIU \right] = \frac{\partial n_a \times \partial \lambda_{\min}}{\partial \lambda_{peak}}$$

5.3.5 Full Width at Half Maximum

The FWHM is the width of the confinement loss curve at half the peak loss. It determines the sharpness of the loss peak. A steeper loss peak improves the sensing capability of a sensor. In addition, FWHM is necessary to calculate the sensor's FOM. As a consequence, while assessing sensor performance, FWHM is an important factor to consider.

5.3.6 Figure of Merit

Aside from AS and WS, the figure of merit is another metric that may be used to estimate sensor efficiency. The only difference is the WS/FWHM ratio. The FOM may be determined using the equation [52], where S_λ represents the WS and FWHM represents the full width at half-maximum.

$$FOM\left[RIU\right] = \frac{S_\lambda}{FWHM}$$

The sensor's sensitivity grows as the FWHM lowers, resulting in a high FOM for a highly performable sensor [56].

5.3.7 Sensor Length

When $\alpha(\lambda, n_a)$ is the peak confinement loss of a given analyte, may be used to determine the length of the sensor for that RI [52]:

$$L\left[cm\right] = \frac{1}{\alpha(\lambda, n_a)}$$

5.3.8 Multiplicative Sensitivity

$$S_m\left[dB/RIU\right] = \frac{\Delta Intensity_{peak} \times \Delta\lambda_{int}}{\Delta n_a}$$

5.3.9 Crest Interference Angle

$$CIA\left[°\right] = 2\tan^{-1}\left(\frac{FWHM}{Intensity_{peak}}\right)$$

5.4 Conclusion

We now have all of the components necessary to construct an SPR-based PCF sensor. We've also learnt how to use the parameters we've learned to assess sensor performance. The next chapters use the characterization equations and performance parameters for these materials to illustrate our proposed sensor architecture and performance.

Chapter 6

Simulation and Experimental Analysis of a square structured Photonic Crystal Fiber based THz sensor design for human body protein detection

6.1 Introduction

The introduction of a squared porous photonic crystal fiber-sensor that may be employed for effective amino acid research employing Terahertz waves is discussed. Detection of amino acids is critical in medical research, notably in medication development. The performance research was performed using FEM and the COMSOL MULTIPHYSICS, and key waveguide characteristics for five necessary amino acids across a broad span of the Terahertz band and diameters of the core were thoroughly evaluated. According to the study's findings, the suggested model has a very high sensitivity (99.98%) and a low confinement loss (4.72×10^{-22} cm^{-1}) for tryptophan, the most scarce of the essential amino acids present in proteins. Two hollow square air holes encircled by four rectangular air pathways in the sheathing provide great sensing capabilities. The sensor is made utilizing an extrusion approach combined with 3D printing, which is also detailed in depth.

6.2 Geometrical Structure and Design Consideration

Figure 6.1 depicts the cross-sectional design of the ZEONEX-based THz PCF sensor, with an expanded perspective of the square hollow core. To build and simulate the proposed photonic crystal fiber sensor, the commercial software COMSOL MULTIPHYSICS-5.3 b was used. Two square holes are surrounded by four equally sized rectangular slots in the cladding construction of this guided PCF. The backdrop material is ZEONEX, while the cladding area is made of air. As previously mentioned, ZEONEX maintains a 1.525 RI throughout a wide range of terahertz bands. ZEONEX is also excellent for our model since this material has a 0.2

cm1 material absorption loss. When it comes to the cladding, the width (W) of the rectangular and square air slots is 342 m. L stands for rectangular air slot length, which is 1820 m, while L1 and L2 stand again for external and internal square air slot length, which are 2616 m and 1422 m, respectively.
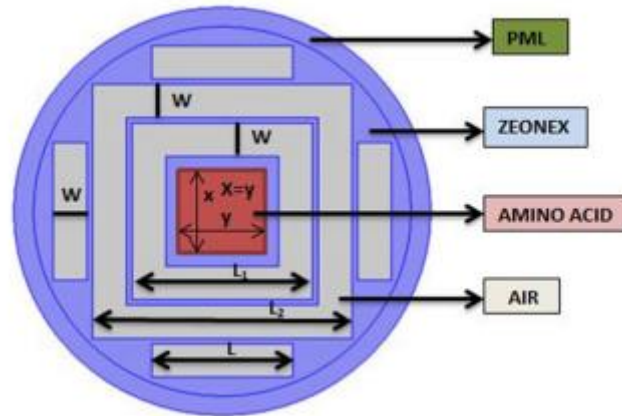
Figure 6.1: Cross section of the proposed terahertz PCF based sensor

The 60-meter distance between the square air holes is established. There are two axes in the core, x and y, which denote the length and breadth of the square-shaped porous core. A hypodermic syringe is used to inject the amino acid analytes into the core. In addition to this, a PML is added to the outside border of the proposed photonic crystal fiber. The purpose of the PML is to prevent light from being reflected and to shield the PCF from the effects of the surrounding environment. It has little practical impact. The thickness of the PML we chose is 9% of the overall radius of the fiber.

6.3 Numerical Investigation of the Proposed Sensor

6.3.1 Fundamental Mode Field scheme

In this suggested framework, user-controlled mesh size was employed to get better outcomes. The whole mesh of the fiber has 3500 parts, 718 boundary components, and 60 edge components, with a degree of flexibility of 24,665 and an average element quality of 0.4735. The suggested photonic crystal fiber is characterized using the well-known finite element technique, or FEM. Microstructure design is converted to a standard differential

component using FEM. FEM is very precise, allowing for the modeling of complicated geometries prior to manufacture as well as comprehensive drawings to help enhance the model. Figure 6.2 shows the fundamental mode field scheme for several amino acid analytes at a frequency of 3.40 THz. The field intensity is strongest at the center and progressively decreases around the radius of the fiber, displaying a Gaussian profile, as shown in the figure. Light has also been tightly constrained into the porous core area, causing the suggested fiber to generate a strong interaction between field and the substance to be felt.
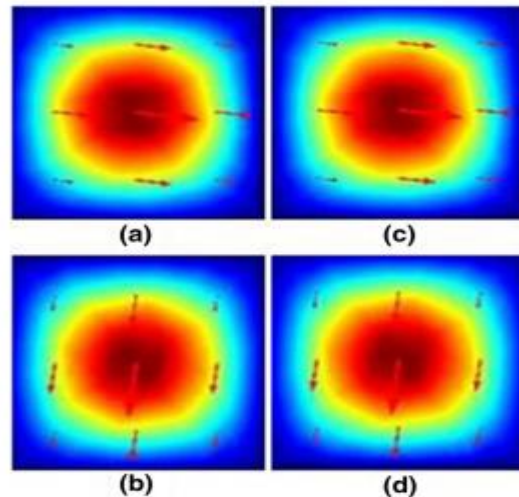
Figure 6.2: Mode field scheme of the proposed fiber for tryptophan and histidine at x-polarization and y-polarizations respectively

As a result, the relative sensitivity of this suggested sensor will be high. We explored the waveguide characteristics in relation to two essential parameters: the THz wave's operating frequency and the core dimension by altering its size. Light is much more effectively confined in the x-polarization mode, which results in a superior relative response and lower confinement loss. As a result, we've decided to ignore the y-polarization mode for the sake of simplicity. The PCF was found to perform best at a frequency of 3.4 THz and a core size of 880 nm, hence these values were selected as the ideal conditions.

6.3.2 Comparative Analysis of Relative Sensitivity with operating frequency and core dimensions

Figure 6.3(a) provides a comparison of relative sensitivity with operating frequency for the four analytes, demonstrating that when the operating frequency is increased, the sensitivity increases gradually and peaks at 3.4 THz, which is the optimal frequency. This is

because higher frequency THz waves are more effective in containing light inside the core [16]. As seen in Fig. 6.3(b), sensitivity increases as core dimensions increase. The bigger core void enables more liquid analytes to be filled, improving the analyte–light interaction in the core and thereby increasing sensitivity.

(a)   **(b)**
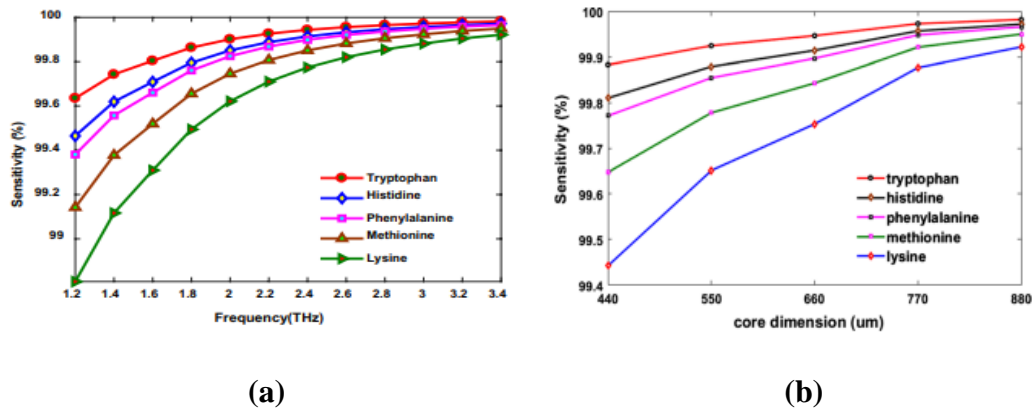
Figure 6.3: Relative sensitivity versus frequency (a) and core dimension (b) graph for different amino acids

At ideal conditions, the sensitivity values for lysine, methionine, phenylalanine, and tryptophan and histidine are 99.93 percent, 99.95 percent, 99.97 percent, and 99.98 percent, respectively.

6.3.3 Analysis of Effective Material Loss

In this comparison, the relative sensitivity of the operational frequency sensing capabilities is compared to each other. The loss mechanism is made up of two parts: EML and CL, with EML taking precedence. EML is shown in Figures 6.4(a) and (b) as a function of frequency of operation and core diameter. The EML diminishes with increasing frequency, as seen in Figure 6.4(a), but the curves plump up as they approach the optimal frequency. The EML has a sharp drop at lower working frequencies, while it is minor at higher frequencies. The analyte within the core has a greater refractive index, which means that high-frequency electromagnetic waves are better able to interact with the amino acid analytes, resulting in low EML [63].
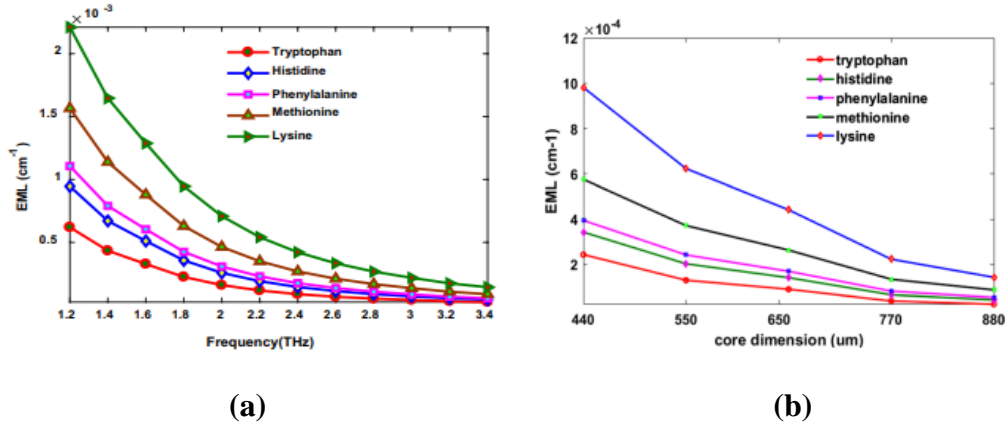
Figure 6.4: EML versus frequency (a) and core dimension (b) graph for different amino acids

The amount of surrounding material that absorbs electromagnetic waves decreases as the core diameter increases, resulting in a drop in the EML, as seen in Fig. 6.4(b) [64]. Under ideal conditions, EML values of 3.33×10^{-5} cm^{-1}, 3.33×10^{-5} cm^{-1}, 6.67×10^{-5} cm^{-1}, 8.33×10^{-5} cm^{-1}, and 1.50×10^{-4} cm^{-1} were obtained from the amino acids tryptophan, histidine, phenylalanine, methionine, and lysine, respectively.

6.3.4 Analysis of Confinement Loss and Effective Area

The CL is another type of loss that we should think about reducing in order to improve the performance of the PCF. When air gaps and holes are inserted, optical power is leaked from the core regions to the outside layers, which results in CL. Figure 6.5(a) shows a plot of confinement loss against frequency, indicating that as the mode field inside the core becomes more confined at higher terahertz frequencies, the confinement loss falls at a variable rate with the increase in operating frequency [65]. Tryptophan, histidine, phenylalanine, methionine, and lysine have confinement loss values of 4.72×10^{-22} cm^{-1}, 1.00×10^{-21} cm^{-1}, 1.90×10^{-20} cm^{-1}, 1.00×10^{-19} cm^{-1}, and 4.60×10^{-19} cm^{-1}, respectively, at 3.4 THz and 880 m.
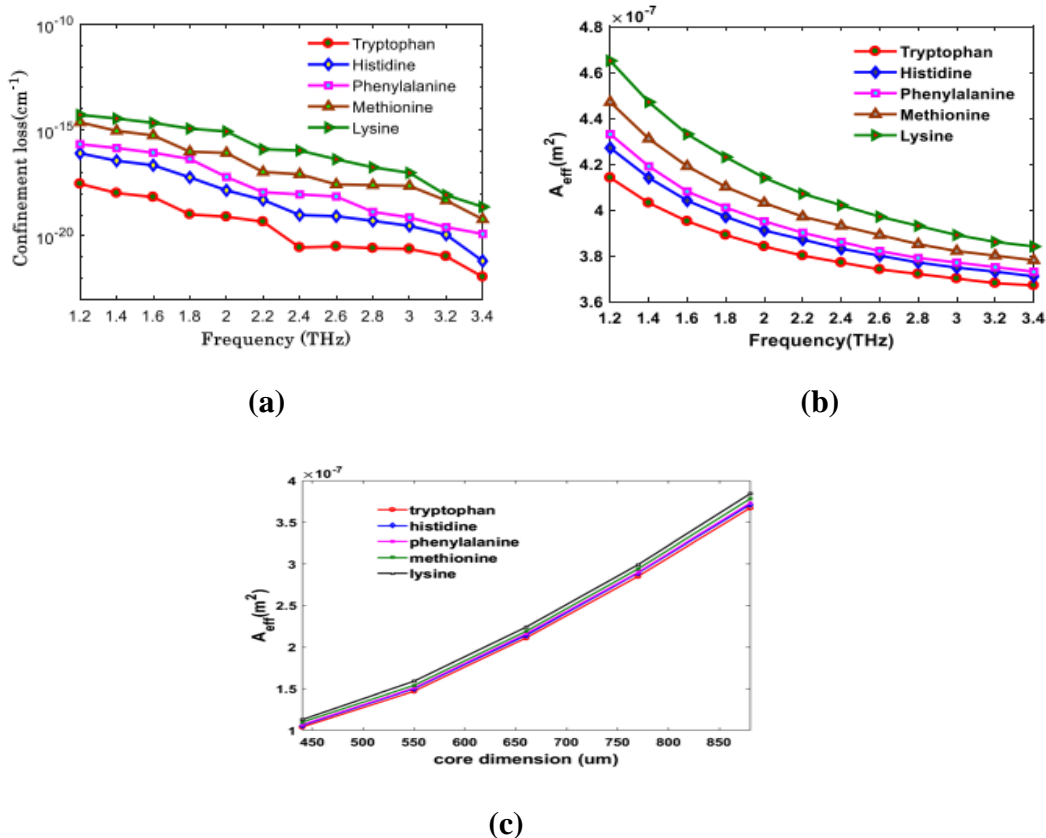
Figure 6.5: Confinement Loss versus frequency (a), Effective area versus frequency (b) and core dimension (c) graph for different amino acids

One of the most important characteristics of PCF sensors is the effective area (EA), defined as the portion of a PCF hollow core where the analyte reacts with the terahertz pulse. According to Fig. 6.5(b), the PCF sensor's effective area decreases as operating frequency increases due to more light being confined in the core region, which is seen in a declining curving pattern. However, the effective area for all amino acid analytes in Fig. 6.5(c) shows an essentially consistent increase with increasing length of the core side. The increase in side length induces an increase in the area of the core and a rise in analyte filling, which results in an increase in the differential RI between the core and the cladding and a reduction in modal area. Leakage power may be recovered from the core by increasing the volume of analyte and decreasing the mode area, resulting in an increase in effective area. Tryptophan, histidine, phenylalanine, methionine, and lysine have effective areas of 3.680×10^{-7} m^2, 3.715×10^{-7} m^2, 3.74×10^{-7} m^2, 3.800×10^{-7} m^2, and 3.840×10^{-7} m^2, respectively.

6.3.5 Analysis of Numerical Aperture and Effective Refractive Index

    The numerical aperture (NA) is another key waveguide parameter that significantly depends on the EA. NA measures the wave confinement capacity within the fiber. The core's RI must be greater than the cladding in order to attain a high NA for medical reasons. The numerical aperture versus operating frequency is shown graphically in Figure 6.6(a). NA follows a similar distribution to the effective area as the EA. Histidine and tryptophan have numerical apertures of 0.084, phenylalanine and methionine have numerical apertures of 0.082, while lysine has a numerical aperture of 0.080.
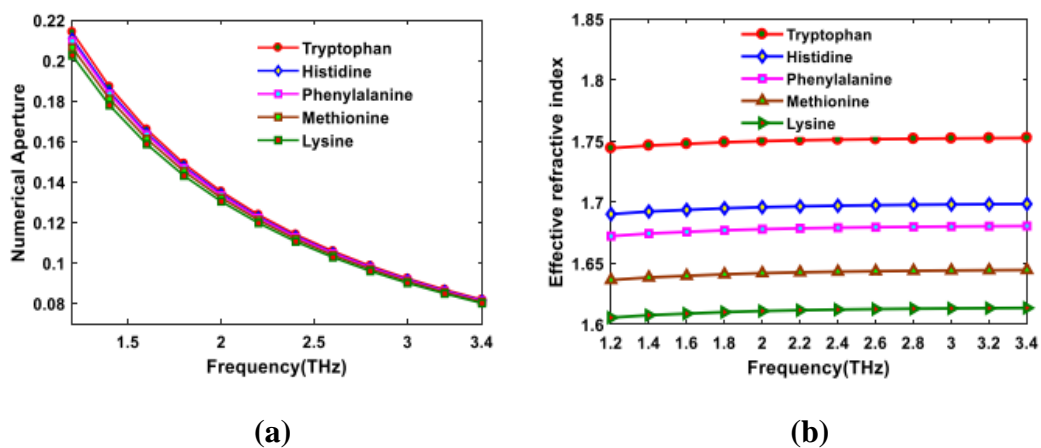
Figure 6.6: Numerical Aperture (a) and Effective Refractive Index (b) versus frequency graph for different amino acids

Fig 6.6(b) shows a minor rise in the effective refractive index as the frequency of operation increases. Enhanced effective RI is caused by shorter wavelengths associated with higher frequencies in EM waves. This phenomenon is amplified when light propagates through an analyte with a higher RI, resulting in a shorter wavelength and an increased effective RI. The fluctuation of the dimension of the core in Fig. 13 shows a similar tendency. More analytes in the core means a greater difference between the core area and the cladding in terms of RIs, which in turn means a higher effective RI [66]. Refractive index values for tryptophan, histidine, and methionine were found to be 1.700, 1.685, 1.63, and 1.620, respectively, in the range of 880–880 micrometers.

6.3.6 Investigation Result at Optimum Conditions

Table 6.1 shows the waveguide parameters at 3.4 THz and 880 nm, the best circumstances after the experiment was completed.

Table 6-1: Summary of the waveguide properties at optimum condition

Optimum conditions: frequency 3.4 THz and 880 μm core dimension

Amino acid	Sensitivity/%	EML/cm^{-1}	Num. aperture	Eff. ref. index	Eff. modal area/m^2	Con. loss/cm^{-1}	Dispersion/ ps/THz/cm
Tryptophan	99.98	3.33×10^{-5}	0.084	1.755	3.680×10^{-7}	4.72×10^{-22}	0.0135
Histidine	99.98	3.33×10^{-5}	0.082	1.700	3.715×10^{-7}	1.00×10^{-21}	0.0150
Phenylalanine	99.97	6.67×10^{-5}	0.082	1.685	3.740×10^{-7}	1.90×10^{-20}	0.0150
Methionine	99.95	8.33×10^{-5}	0.082	1.643	3.800×10^{-7}	1.00×10^{-19}	0.0150
Lysine	99.93	1.50×10^{-4}	0.080	1.620	3.840×10^{-7}	4.60×10^{-19}	0.0180

Observed sensitivity, total loss, and dispersion are all much lower for the proposed model than for any of the other preceding models at their respective optimal values, as the table shows.

6.4 Conclusion

In this work, we propose a square hollow core PCF biosensor for detecting four key amino acids. For tryptophan and histidine, the relative sensitivity of the presented sensor model is 99.98 percent, phenylalanine is 99.97 percent, methionine is 99.95 percent, and lysine is 99.93 percent. At ideal design settings of 3.4 THz and 880 m, further noteworthy propagation properties for the analytes were discovered, including low confinement and effective material loss, high effective modal area, and near-zero fat dispersion. The method works effectively for detecting amino acids and other biomolecules, especially tryptophan, the rarest of the essential amino acids. Complex cross-sectional design was used to achieve this better performance, although extrusion methods, 3D printing, and other new methodologies might also be used. In addition, the near-zero fat distribution provides great opportunities in the telecommunications business. The provided PCF model will undoubtedly be useful in the realm of bio-sensing.

Chapter 7

Simulation and Experimental Analysis of hexagonal outlined porous cladding with vacant core photonic crystal fiber biosensor for cyanide detection at THz regime

7.1 Introduction

A hexagonal outlined porous cladding with an unoccupied core photonic crystal fiber (HOPCVC PCF) sensor has been developed using Zeonex to detect cyanides in the THz domain. Cyanides are extremely dangerous to humans because they can kill them quickly. To avert disability or fatality, such hazardous chemicals must be discovered promptly. For the current proposal, three alternative THz regimes were studied. The FEM is used to investigate various analytes quantitatively. The results of the simulation reveal that at the best design choices, very high levels of 99.75% sensitivity, 0.5×10^{-13} cm^{-1} confinement loss, and minimal and uniform 0.12 ps THz/cm dispersion, as well as other notable properties, were achieved.

Analysis and design techniques have been clearly explained. Modern technology can easily construct the model due to its basic shape. In addition to chemical uses, its excellent sensing capabilities will allow it to be used in other industries as well. They will, however, play a significant role in other applications.

7.2 Geometrical Structure and Design Consideration

The model's cross section and three-dimensional viewpoint are shown in Figure 7.1. The outcome is a hexagonally defined hollow cladding with an empty core PCF (HOPCVCPCF), which has 54 air holes in total. The hexagon's whole geometry is asymmetric, which helps the PCF attain significant birefringence. An empty core sits between layers of square-shaped air holes in the hexagonal cladding area. The first layer has 12 air slots; the

second layer has 18 slots; and the third layer has 24 slots. It is common practice to use porous cladding to reduce the cladding's RI in this way. Zeonex background material in the cladding zone is reduced even more by using squared air openings rather than circular, oval, or other kinds of air venting. Each cladding air gap in our model has equal lengths on both sides.
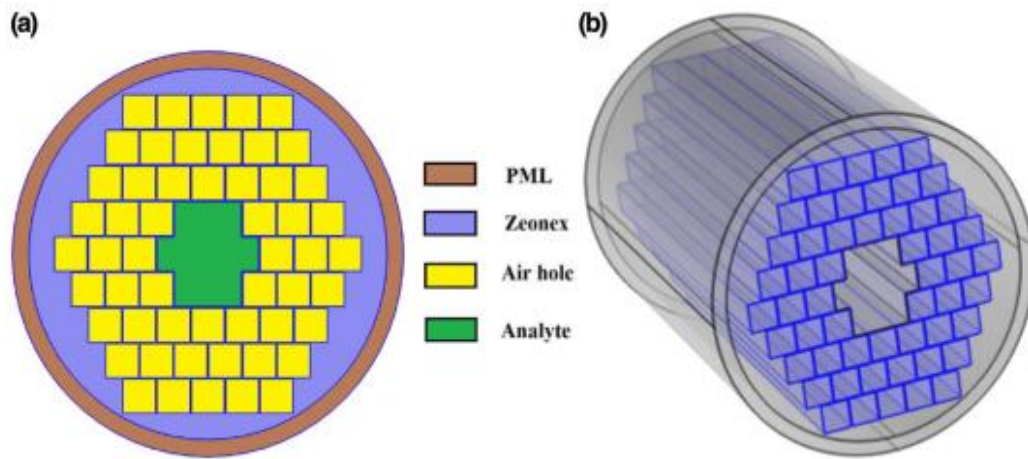
Figure 7.1: (a) Cross-sectional view and (b) 3D view of the proposed sensor with Zeonex as the background substance

The air hole diameter and strut width are dependent on this. As we observed in our study, sensitivity, EML, NA, and EA all impact side length and therefore PCF performance. In spite of the fact that narrowing the struts would increase performance, a minimum strut width must be maintained in order to retain the structural stiffness of PCF. The middle of the core is hollowed out by eliminating seven air holes. When analyte fluid samples are added to the empty core, the effective refractive index of the core area exceeds that of the cladding region, resulting in a larger effective RI in the core than in the cladding region. As previously noted, Zeonex was chosen as the model's structural material since its RI of 1.53 stays constant across a large frequency range [67],[68]. As a result, chromatic dispersion's effects are greatly reduced. The cladding region has also had a PML built around it to establish boundary parameters for computing CL. Background material was considered to have the same quality in all directions for the simulation. The use of an isotropic material facilitates the computation and cuts down on the time it takes to complete.

7.3 Analysis of Sensor Performance

7.3.1 Fundamental Mode Field scheme

The mode distributions for the three analytes in this constructed PCF are shown in Figure 7.2. An empty hollow core may be seen as a Gaussian profile, with the mode field condensed into this area by its radial location from its center. With reduced loss of wave power, THz waves may be able to interact with analytes more efficiently, resulting in improved sensitivity.
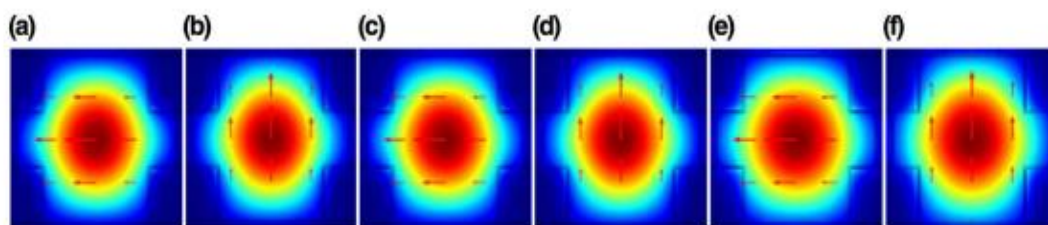
Figure 7.2: L Mode distributions for NaCN, KCN and HCN as analyte

Additionally, the RI gap between the cladding and the core narrows when the refractive indexes of analytes decrease. Following that, as seen in Figure 7.2, the mode field tends to scatter towards the cladding. Furthermore, the x axis confinement is significantly tighter than the y axis. For this reason, birefringence is enhanced by the asymmetrical cladding structure.

7.3.2 Analysis of Sensitivity

At the ideal side length and strut size, Figure 7.3(a) demonstrates how sensitivity evolves with frequency. Raising the frequency till 2.3 THz improves sensitivity significantly, after which there are no discernible variations. This characteristic is similar to that mentioned in Ref. [19]. In the 1.0 THz range, the sensitivity of NaCN (98.5%), KCN (98.5%), and HCN (98.5%) is measured. When frequency is increased, both P and n_{eff} rise. As a consequence, core power and relative sensitivity are proportionate. P increases as frequency decreases, but the core power percentage stabilizes at about 2.3 THz, resulting in a flat curve beyond the ideal frequency. This means that high-frequency light is limited within the core [4].

Because wavelengths go longer, more of the wave power doesn't combine with the analyte, leading to a decreased sensitivity as a result of the light broadening.

Figure 7.3: Graphical representation of sensitivity versus (a) frequency, (b) side length, and (c) strut size for different analyte

The achieved sensitivity for NaCN, KCN, and HCN at the ideal 2.3 Terahertz was 99.75 percent, 99.5 percent, and 98.0 percent, respectively. The sensitivity rises as the side length increases, as seen in Figure 3b.Figure 3c shows that increasing strut size lowers the optical wave power in the core, resulting in a fall in core power fraction and a loss in sensitivity.

7.3.3 Analysis of Confinement Loss

Figure 7.4(a) depicts the relationship between CL and operating frequency. The confinement loss decreases with increasing frequency; for example, with HCN, the CL decreases from 0.50 cm^{-1} to 1.0×10^{-12} cm^{-1} by shifting frequency from 1.0 THz to 2.3 THz. As frequency rises, the mode fields tend to become more focused near the core region [65]. At 2.3 THz (optimum frequency), the confinement losses for NaCN, KCN, and HCN are 0.5×10^{-13} cm^{-1}, 0.4×10^{-13} cm^{-1}, and 1.0×10^{-12} cm^{-1}, respectively.
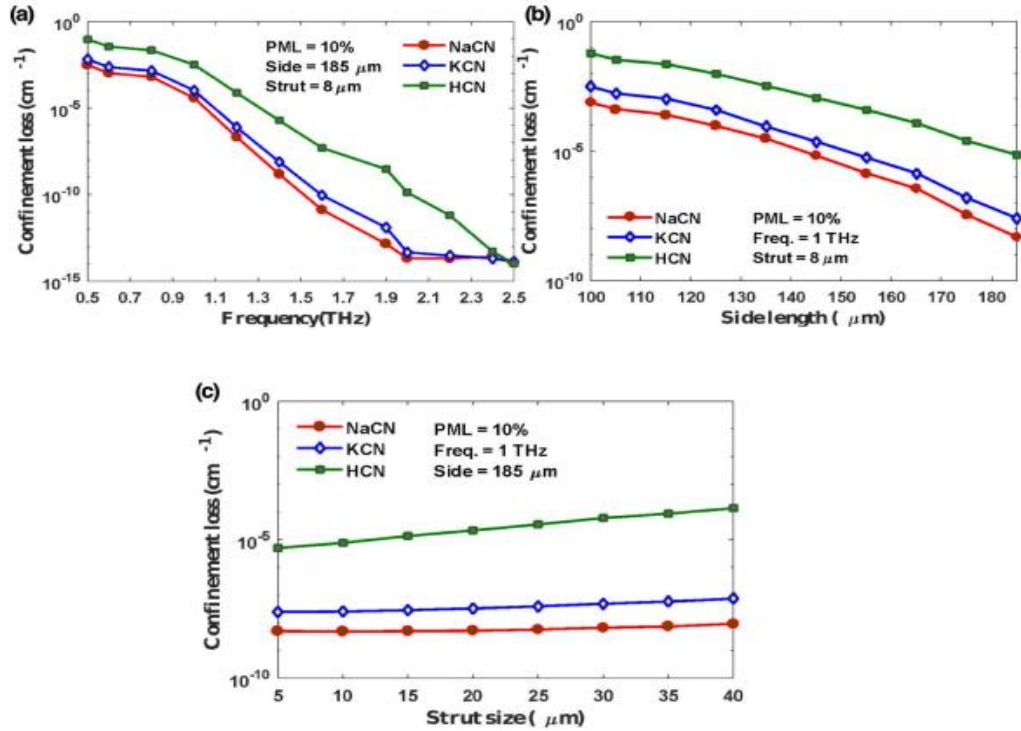
Figure 7.4: Graphical representation of confinement loss versus (a) frequency, (b) side length, and (c) strut size for different analyte

Figures 7.4(b) and (c) show how strut size and side length affect confinement loss. Because of the increasing porosity of the cladding, the confinement loss decreases as the side length rises, as shown in 7.4(b). Because strut size and side length are inversely related, as shown in Figure 7.4(c), confinement loss should rise as strut size increases.

7.3.4 Analysis of Effective Material Loss

Figure 7.5(a) depicts the EML's frequency-dependent variation. As frequency rises, EML drops. Lower THz frequencies (0.5 THz–1.8 THz) see a sharp decline, whereas higher THz frequencies (over 1.80 THz) see a more steady decline. When HCN was used as the analyte, the sensor's EML amplitude was 2.5 103 cm1, but this dropped to 1.4×10^{-3} cm^{-1} when it attained peak performance. The research report in Ref. [69][18] backs up this EML tendency. The EML values obtained at the ideal frequency of 2.30 THz for NaCN, KCN, and HCN are 0.5×10^{-3} cm^{-1}, 0.6×10^{-3} cm^{-1}, and $1. \times 10^{-3}$ cm^{-1}, respectively.
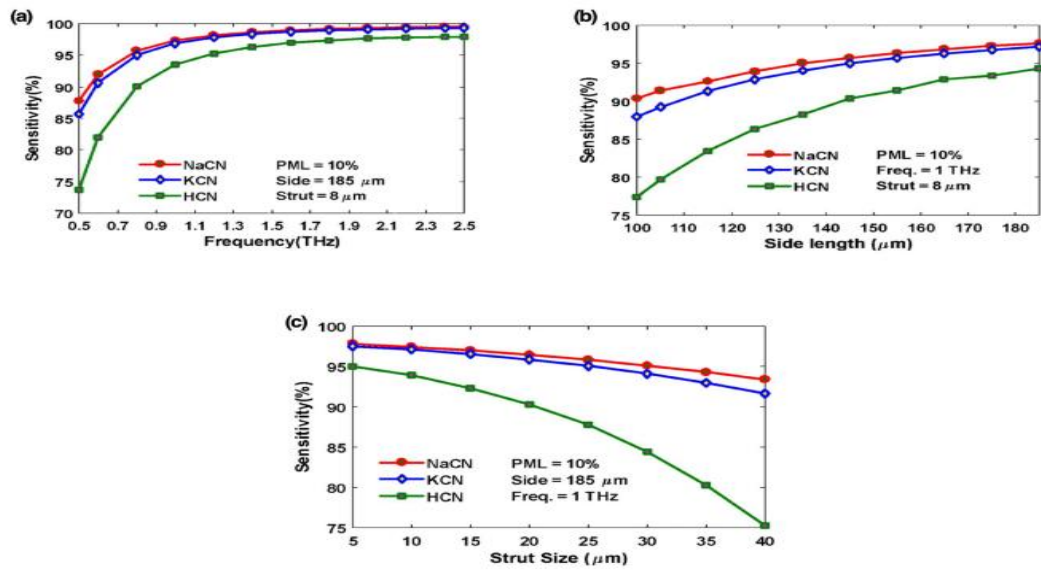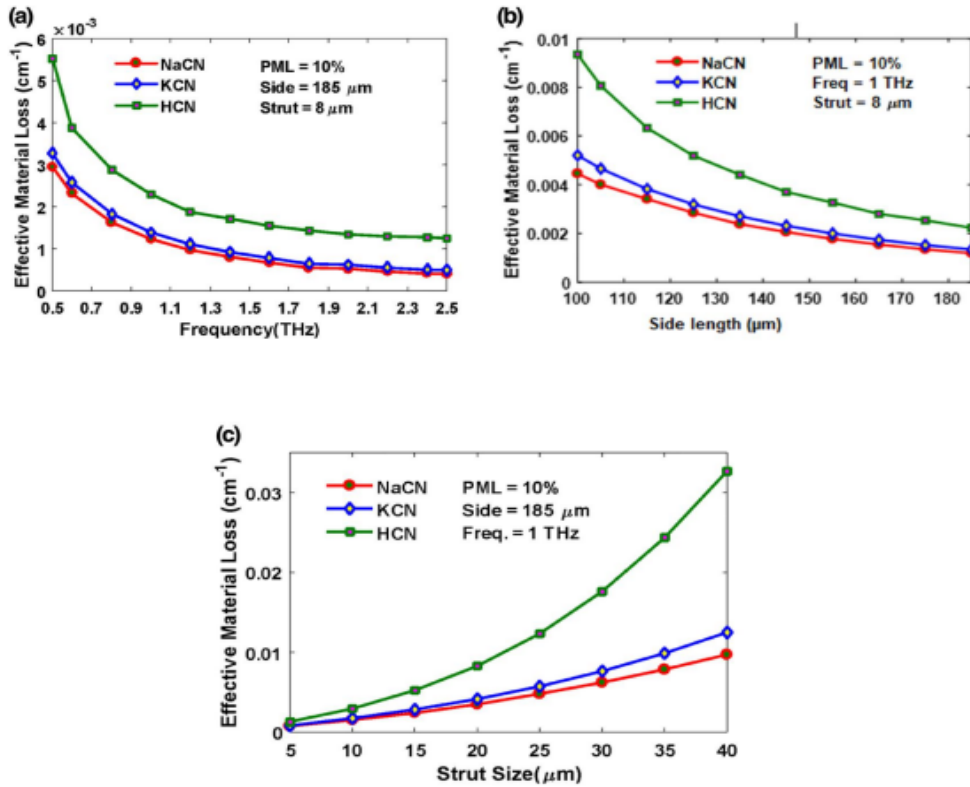
Figure 7.5: Graphical representation of EML versus (a) frequency, (b) side length, and (c) strut size for different analyte

To illustrate how side length and strut size affect EML, Figures 7.5(b) and (c) show the results. The EML diminishes as the side length rises, as seen in Figure 7.5(b). More air holes result from longer side lengths, which means less background material is utilized in the core area and the EML is lowered. The EML rises with strut size, as seen in Figure 7.5(c).

7.3.5 Analysis of Dispersion

For ideal strut size and side length, the dispersion variation with frequency is shown in Figure 7.6. It has been observed that as frequency rises, so does dispersion.
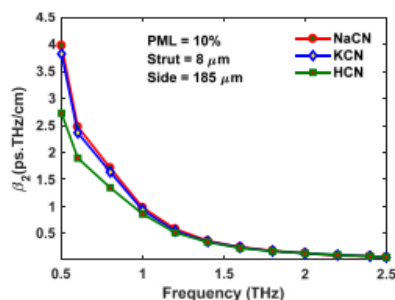
Figure 7.6: Graphical representation of dispersion versus frequency for different analytes

At frequencies ranging from 2.1 to 2.5 terahertz, a super-flat dispersion range of around $0.12\pm$ 0.05 ps.THz/cm can be produced for analytes, and the optimum dispersion is around 0.12 ps.THz/cm.

7.3.6 Investigation Result at Optimum Conditions

We've summarized our findings from an investigation of optimum sensor performance in Table 7.1. According to our calculations, this sensor's effective area is almost as large as the whole core area when used at its optimum frequency. A remarkable interaction between the analytes and the THz waves was seen because the core-guided modes were firmly contained within the core.

Table 7-1: Synopsis of the performance analysis of the proposed sensor

At optimum values (Frequency = 2.30 THz, side length = 185 µm, and strut size = 8 µm)

Analytes	Confinement loss (cm^{-1})	Sensitivity %	Effective material loss (cm^{-1})	Effective modal area (m^2)	Numerical aperture	Dispersion (ps.THz/cm)
HCN	1.0×10^{-12}	98.0	0.5×10^{-3}	1.65×10^{-7}	0.175	0.12
KCN	0.6×10^{-13}	99.50	0.6×10^{-3}	1.50×10^{-7}	0.20	0.12
NaCN	0.5×10^{-13}	99.75	1.4×10^{-3}	1.35×10^{-7}	0.21	0.12

The excellent sensitivity response was due to these three criteria for all of the analytes examined. Furthermore, from 2.0 THz to 2.5 THz, the suggested model yielded a very flat dispersion.

7.4 Conclusion

For THz sensing, a Zeonex-based HOPCVCPCF is designed in this research. The empty core is intended to optimize the analyte's interaction with the THz pulse while minimizing material loss. The proposed model was evaluated at frequencies spanning from 0.5 to 2.5 THz. When the ideal design parameters were employed, an ultra-flat confinement loss of around 1.0×10^{-12} cm^{-1} was generated using HCN, 0.6×10^{-13} cm^{-1} using KCN, and $0.5 \times 10^{-}$

^{13} cm^{-1} using NaCN. Most importantly, the sensitivity of the HCN, KCN, and NaCN refractive indices was found to be 98.0 percent, 99.50 percent, and 99.75 percent, respectively. Aside from these enticing characteristics, the proposed model exhibits a near-zero flat dispersion, minimal material loss, and a large mode area. Because of its remarkable characteristics, easy design, and manufacturing possibilities, the model is suited for identifying harmful chemicals. It is intended to make substantial contributions to photonics and THz research in a variety of domains.

Chapter 8

Simulation and Experimental Analysis of Quad Channel SPR based PCF Sensor for Analyte, Strain, Temperature and Magnetic Field Strength Sensing

8.1 Introduction

Based on surface plasmon resonance, this work offers a simple, fabrication-friendly, very low-loss photonic crystal fiber sensor. We use a di-material plasmonic coating of 20 nm gold and 10 nm titanium dioxide in our suggested sensor. Comsol Multiphysics V 5.5 use the finite element method (FEM) to detect changes in the sensor's optical characteristics. After optimizing all cross-sectional parameters, the sensor model achieved maximum Amplitude Sensitivity (AS) and Wavelength Sensitivity (WS) for unknown analyte sensing of 4646.1 RIU^{-1} and 10,000 nm/RIU, respectively, with sensor resolutions of 2.15×10^{-6} RIU and 1.00×10^{-5} RIU within the 1.33-1.42 RI range. In addition, at 1.43 RI, a very low maximum confinement loss magnitude of 0.8125 dB/cm was reported. Furthermore, in terms of strain, temperature, and magnetic field strength, unusually high maximum sensitivities of 0.004 nm/$\mu\xi$, 1.00 nm/C, and 0.16 nm/Oe were found. Our suggested sensor is unique in its ability to detect unknown analytes, strain, temperature, and MFS.

8.2 Structural Design and Theoretical Modeling

The performance of a PCF sensor is mostly determined by its design. It affects both the core's light direction characteristic and the optical power provided to the plasmonic mode. A cross-section of the suggested PCF sensor model is shown in Figure 8.1. For the backdrop, fused silica was employed. The building has a solid core in the center and cladding on all four sides. The cladding is made up of air holes with a diameter of d_1 that are close together to form a cluster of two to four air holes as you go out from the center. The solid center is surrounded

by four clusters. These composite air holes serve to guide light inside the core, limit excessive light dispersion from the core, and transfer optical power throughout the four channels.
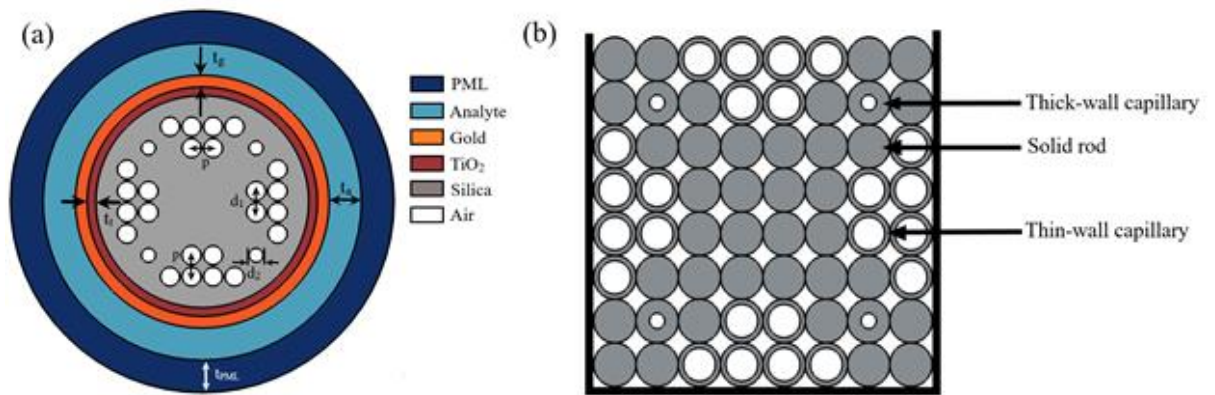
Figure 8.1: (a) The cross-section of the proposed sensor, (b) stacked framework of the design

The pitch is the distance between the centers of one air hole and the next air hole in the cluster which is set at 1.0 m [70]. According to the previously given data, the diameter of d_2 is 0.65 m. A layer of TiO2 with a thickness of t_t was placed on the PCF structure, followed by a t_g gold layer. The high conductivity of gold enables surface plasmon waves. The TiO2 layer acts as a protective layer between the gold and the silica. The analyte layer, ta, is chosen at random at 1.5 m. An artificial perfectly matched layer (PML) has been created around the whole structure for simulation purposes only, with the intention of replicating boundary conditions and absorbing any energy discharging out. The optimal structural parameters after study are $d_1 =$ 0.95 m, $t_g = 20$ nm, and $t_t = 10$ nm.

8.3 Sensor Performance Investigation and Optimization of Different Geometrical Parameters

8.3.1 Field Guiding Properties

Figure 8.2(a) and (b) demonstrate the field pattern caused by the core-guided mode for the x and y polarizations.
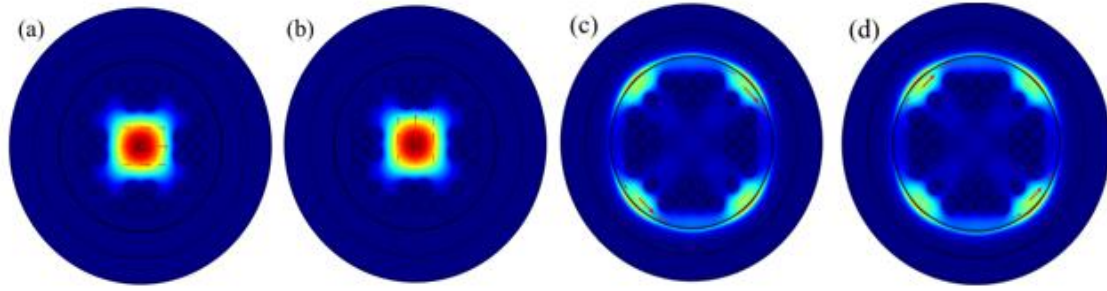
Figure 8.2: Optical field pattern due to the core-guided mode and the Surface Plasmon mode at both polarizations

The core region was light-restricted, and the four cross-sectional channels allowed leaky fields to diffuse into the cladding and interact strongly with the plasmonic material, as seen in Figs. 8.2(c) and (d). As a result, the plasmonic region's power and the sensor's outgoing power have been kept in good balance.

8.3.2 Refractive Index Optimization

By tailoring the sensor cross-sectional characteristics, the key component of successful detection of unknown analytes is accomplished. The bigger the change in confinement loss and the shift in the resonant peak, the better the detection accuracy. Intermediate RIs between discrete RI values would likewise be easier to discern. Figure 8.3(a) shows the confinement loss spectra for the RI detection range for x polarization, whereas Figure 8.3(b) shows the corresponding amplitude sensitivity. The detection range is selected at RI 1.33–1.42, based on biochemical investigations and observations of irregularities in loss spectra as well as peak broadening [50]. As the analyte RI rises, the resonant peak redshifts, as seen in the figures. The little increase in the plasmonic zone's RI reduces the effective index difference between the core and cladding, enabling a higher proportion of core power to pass through to the plasmonic area.
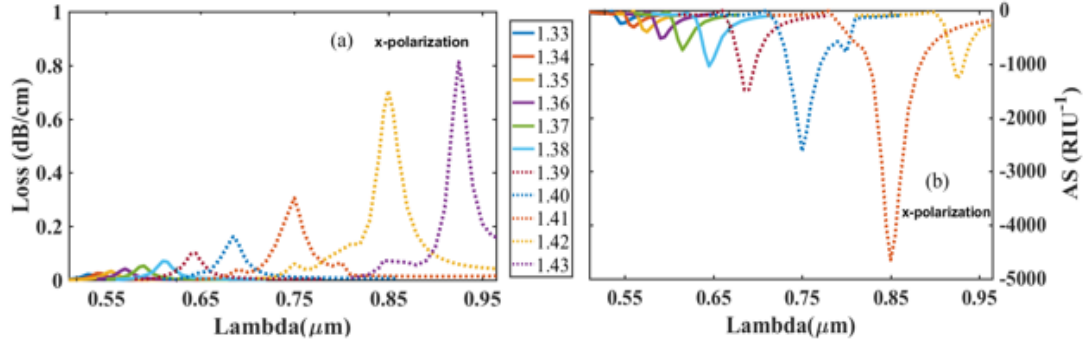
Figure 8.3: Confinement loss spectra (a) and corresponding Amplitude sensitivity (b) for analyte RI array of 1.33-1.43

With an average wavelength sensitivity of 3950 nm/RIU and a maximum wavelength sensitivity of 10000 nm/RIU, the sensor had the greatest peak shift and peak amplitude sensitivity at RI of 1.41. Furthermore, the proposed sensor has an extremely high maximum wavelength resolution of 1×10^{-5} RIU, implying that changes in the proposed sensor might detect very minor changes in RI of the order of 10^{-5}, assuming a spectral resolution of 0.1 nm. As the amplitude sensitivity in Fig. 8.3(b) approaches higher RIs, its magnitude increases significantly until it truncates at RI 1.42 with peak broadening. With an average AS of 1326.6 RIU^{-1}, the maximum amplitude sensitivity was 4646.09 RIU^{-1}, and the highest AS resolution was 2.15×10^{-6} RIU at 1.41 RI.

8.3.3 Optimization of Gold Layer Thickness

A di-material plasmonic zone is formed by two layers of gold and titanium dioxide in the plasmonic region. Gold is one of the most conductive metals, and its abundant surface electrons make it simpler to generate surface plasmon waves.

Figure 8.4: Confinement loss spectra (a) and corresponding Amplitude sensitivity (b) for gold layer thickness, t_g, variation

Figure 8.4 shows how the gold layer thickness affects the sensor's performance. As gold thickness grows in (a) and (b), the resonance wavelength shifts to higher values. The loss peak climbs steadily at the same period, while the amplitude sensitivity peaks at 20 nm thickness before plummeting. The very thin gold film (15 nm), on the other hand, is more vulnerable to the skin depth effect, resulting in low sensitivity [71].

8.3.4 Optimization of TiO$_2$ Layer Thickness

However, gold fails to attach to dielectric surfaces, despite its extraordinary plasmonic properties. To prevent the gold coating from flaking off during use, a TiO$_2$ layer is placed between it and the dielectric surface. The sensor performance as a function of TiO$_2$ thickness (t_t) is shown in Figures 8.5(a) and (b). Concealment loss rises as the TiO2 layer thickness increases, according to the loss spectra. The peak sensitivity, however, stops increasing around 10 nm due to inadequate interaction of the evanescent field with the analyte.
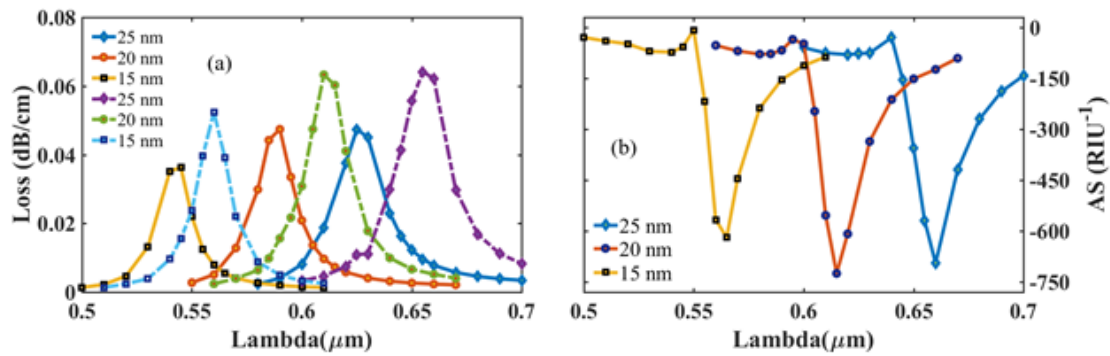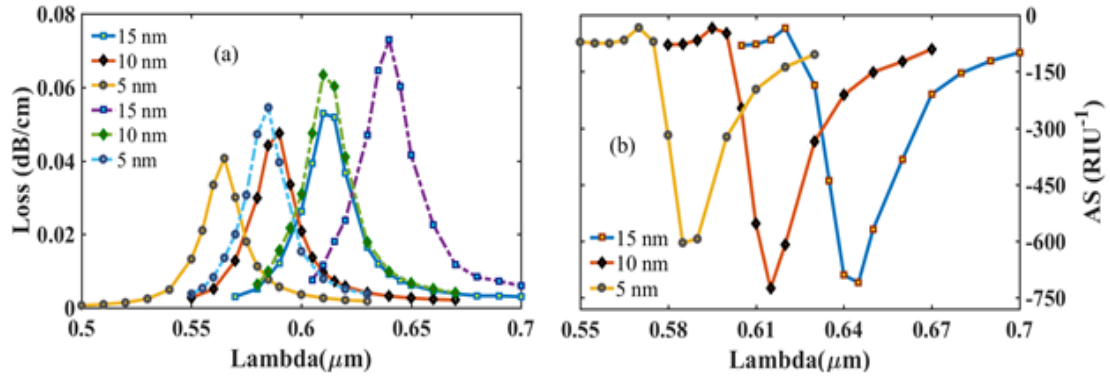
Figure 8.5: Confinement loss spectra (a) and corresponding Amplitude sensitivity (b) for TiO2 layer thickness, tt, variation

Furthermore, since a larger layer results in a bigger loss peak, a thinner layer is selected for excellent peak sharpness and high sensitivity. After considering everything, ideal values of 20 nm and 10 nm for t_g and t_t are determined for further parameter optimization.

8.3.5 Optimization of the air-hole diameter (d1)

The clustered air hole configuration with a d_1 diameter restricts wave power in the core while enabling leaky mode powers to stream into the cladding and then into the plasmonic region through the specified channels. Because there are no changes in the plasmonic region, variations in air-hole diameters do not induce resonant wavelength shifts.
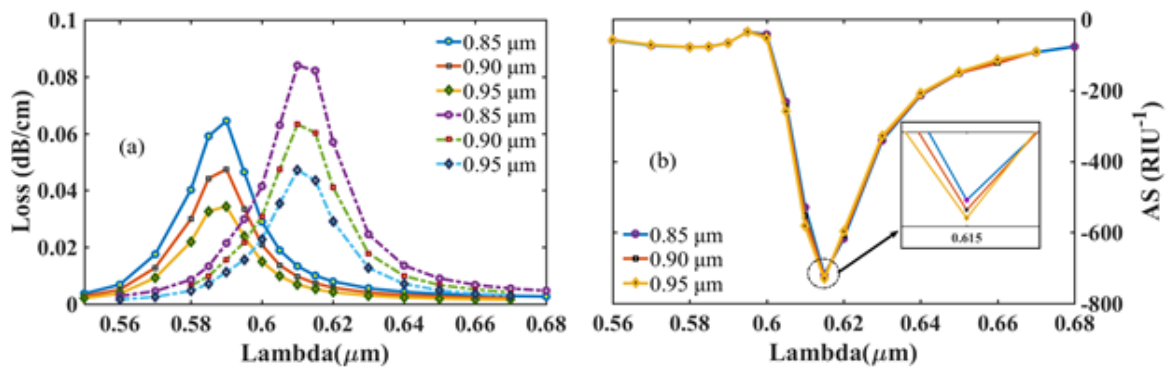

Figure 8.6: Confinement loss spectra (a) and corresponding Amplitude sensitivity (b) for d1 variation

As demonstrated in Fig. 8.6(a) and (b), the major purpose of air-hole optimization is to produce a finer improvement in confinement loss and sensitivity. According to our results, raising d_1

from 0.90 to 0.95 µm improved sensitivity the most; hence, 0.95 µm was selected as the optimal value.

8.3.6 Sensor Performance Analysis at Optimized Parameters

Because many biological and biochemical solvents have RIs in this range, we intended to develop a system that could detect analytes with RIs between 1.33 and 1.42. Ethanol has a refractive index of 1.361 and acetone has a refractive index of 1.36. These are only a handful of the hundreds of compounds detected by the sensor model. Table 8.1 summarizes the results of the performance analysis.

Table 8-1: Summary of overall sensor performance for given refractive index range

RI	λ_{peak} (nm)	α_{peak} (dB/cm)	Ampl. Sensitivity (RIU^{-1})	Resolution (Ampl.) ($\times 10^{-6}$)	Wavel. Sensitivity (nm/RIU) ($\times 10^3$)	Resolution (Wavel.) ($\times 10^{-6}$)	FWHM	FOM
1.33	530	0.021	243	41.1	1.0	100	18.4	54.4
1.34	540	0.025	308.8	32.4	1.5	66.7	19.2	77.9
1.35	555	0.033	395.7	25.3	1.5	66.7	18.8	80
1.36	570	0.042	519.5	19.2	2.0	50	19.4	103
1.37	590	0.053	735.9	13.6	2.0	50	20.6	96.9
1.38	610	0.071	1037.9	9.64	3.5	28.6	22.2	158
1.39	645	0.101	1481.8	6.75	4.0	25	24	166.4
1.40	685	0.162	2624.2	3.81	6.5	15.4	26.3	247.6
1.41	750	0.306	4646.1	2.15	10	10	28.8	346.7
1.42	850	0.707	1272.4	7.86	7.5	13.3	28.7	261
1.43	925	0.813	-	-		-	-	-

8.3.7 Temperature Response Investigation

It is the basis of the sensor's temperature response and will most likely be used in an environment with varying temperatures. The melting point of ethanol is -114.1°C and the boiling point is 78.37°C; the RI limit of ethanol at these temperatures is 1.403–1.343, which

matches within the RI detection array of the proposed model. As a consequence, it is the best alternative for our research.
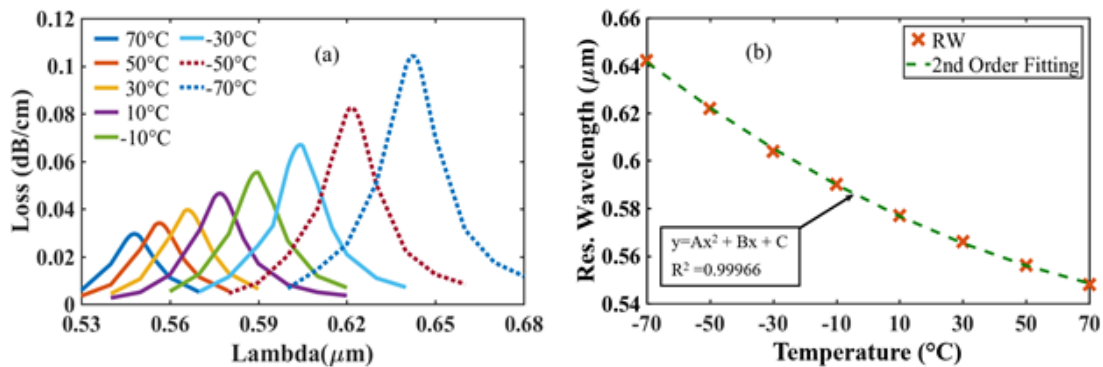
Figure 8.7: Confinement loss pattern (a) for ethanol and Curve fitting (b) of resonant wavelength against the temperature

Figure 8.7(a) depicts the loss spectra for ethanol at different temperatures. As the temperature decreases, the RI of ethanol increases, enabling more core mode power to leak into the cladding. Fig 8.7(b) shows the fitting curve between the resonant wavelength and temperature. Using proper formulas with a spectral resolution of 0.1 nm, the peak temperature sensitivity and resolution were 1.0 nm/C and 0.10 nm/C, respectively. Because of the excellent performance values and the expanded regression equation, the sensor model is suitable for temperature sensing.

8.3.8 Strain Response Investigation

The ability of SPR-PCF sensors to detect extremely small external loads has been shown. The fused silica changes its overall refractive index when subjected to minute stresses, making it easier to identify micro-strains in the PCF structure. Strain, on the other hand, has no effect on the optical properties of the analyte, the plasmonic layer material, or the air in the cavities. With 1.41 analyte RI, we varied the applied external strain from 0 to 2000, and the resulting loss spectra are presented in Fig. 8.8(a). The RI of fused silica decreases as applied strain increases. Figure 8.8(b) shows the linear curve fitting of the resonant wavelength as a function of applied strain.
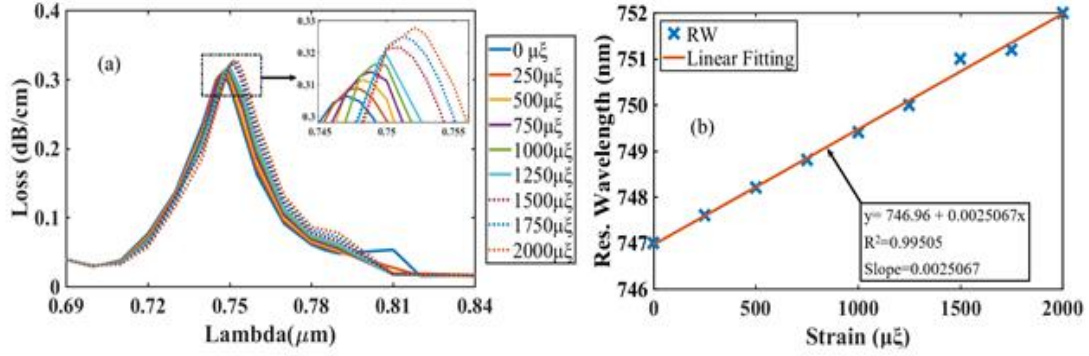
Figure 8.8: Confinement loss pattern (a) and regression line of resonant wavelength (b) with applied strain

The sensor model's total strain sensitivity is represented by the slope of the graph, which is 0.0025067 nm/μξ or 2.5067 pm/ μξ. According to this, the resonance wavelength moves by 2.5067 pm per unit change micro-strains.

8.4 Conclusion

An SPR-based PCF sensor with low loss and appropriate sensitivity has been proposed and researched. A well-matched layer keeps the EM pulse confined inside the fiber. The full vectorial finite element approach is used to do numerical computations. Spheroid air holes are employed to make the external sensing approach manufacturing friendly. To get the best results, we fine-tuned all of the optical parameters. The sensor type has a very low peak confinement loss of 0.8125 dB/cm, with a maximum AS of 4646.1 RIU^{-1} and 2.15×10^{-6} RIU resolution, and a maximum WS of 10,000 nm/RIU and 1.00×10^{-5} RIU resolution. Our sensor has a very high external strain sensitivity of 2.5067 pm/μξ, in addition to magnetic field and temperature sensing potentials.

Chapter 9

Proposed Design: PCF based Mach Zehnder Interferometer through Surface Plasmon Mode Splitting Phenomenon

9.1 Introduction

In this chapter, we have discussed our proposed our PCF based refractive index sensor. The sensor has been modelled in the 3D space dimension of the commercially available COMSOL Multiphysics v5.5, which utilizes the renowned FEM. Moreover; several sensing parameters have also been investigated to determine the sensor performance. The sensor's interferometer section comprises a doped silica layer and then a plasmonic gold layer. Through wavelength interrogation method and optimizing the geometric parameters, it is revealed that the proposed sensor model exhibits a very high sensitivity of 14.152 dB/RIU and crest interference angle of 8.8 at analyte refractive index of 1.44. The PCF cross-section has been designed keeping in mind the feasibility of the fabrication process. The sensor can detect analytes with a very high refractive index, in 1.44-1.52. The proposed model is proficient in detecting a wide range of organic liquids like Chloroform (1.44), Glycerin (1.47), Paraffin (1.48), Toluene (1.47), Benzene (1.50) etc. Additionally, many blood components include Bovine Serum Albumin (1.470), Polyacrylamide (1.452), Biotin-Streptavidin (1.450) and many more. Hence, it is explicit that our proposed sensor model will have a significant impact in analyte sensing not only in organic chemical industries but also in the medical sector as well.

9.2 Proposed Sensor Design

The proposed MZI sensor comprises Single-mode fiber-Photonic Crystal fibre -Single-mode fibre (SMF-PCF-SMF) arrangement as depicted in figure 9.1. The PCF acts as the main interferometer.
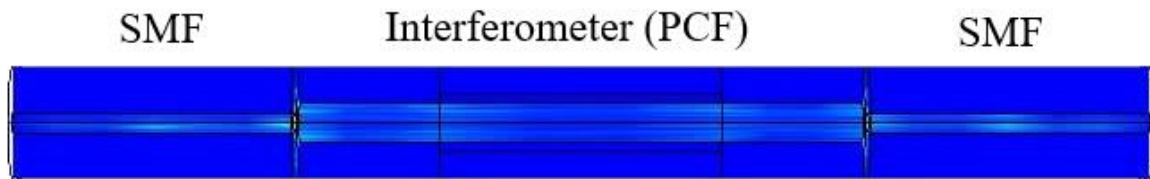
Figure 9.1: Longitudinal Section of the proposed Sensor

The materials used for respective sections of the design:

Input-Output SMF:

- Silica is used as the core
- Silicon is utilized for the cladding.

PCF:

- Silica is used for the core.
- Thin Doped silica for cladding
- Gold as the plasmonic layer

The Gold and Doped Silica layer creates an inner metal-insulator interface while the analyte and gold layer forms the outer metal-insulator region.

For practicality, a constant refractive index of the constituent materials is not used. Instead, the gold layer is modelled using the Drude Lorentz model, while respective wavelength-dependent refractive equations are used for the other materials.

A metastable surface plasmon mode is generated when a guiding mode travelling through the SMF passes through the PCF[72]. Due to the difference between the respective refractive indices of the two metal-insulator regions, the generated surface plasmon mode splits into two modes: the inner SPP and the outer SPP modes. At the end of the interferometer, the two SPP modes recouple back, and due to the slight path difference, the interference occurs with changing wavelengths. Figure_ shows the cross-section of the sensor with the core guided mode in the SMF and the inner SPP mode in the PCF.
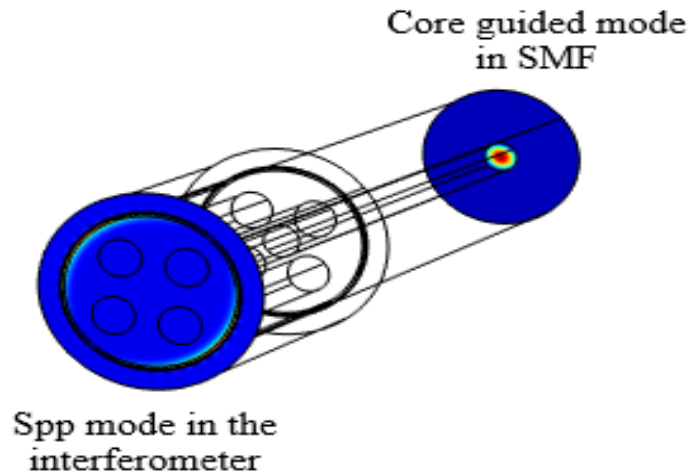
Figure 9.2: Cross-sectional view of the proffered sensor

Observing through the cross-section of the PCF, four large air holes are placed diagonally in the cladding, keeping in mind the simplicity of fabrication and the novelty of the work. Our investigation has optimized several structural parameters to obtain the best sensitivity. The structural dimensions optimized are sensor length (l_{pcf}), gold layer thickness (t_g) and doped silica layer thickness (t_s). Starting from arbitrary values, the maximum sensitivity achieved was 14.152 dB/RIU from an initial magnitude of 5.379 dB/RIU at 1.44 analyte RI.

9.3 Performance Analysis of the proposed sensor with optimization of structural parameters

9.3.1 Intensity Interrogation

The main objective of our sensor is to be sensitive to changes in analyte refractive indices. Before performing the wavelength interrogation, it is necessary to carry out the Intensity Interrogation to check this authenticity. Figure 9.3 shows the graphical representation of the analysis.
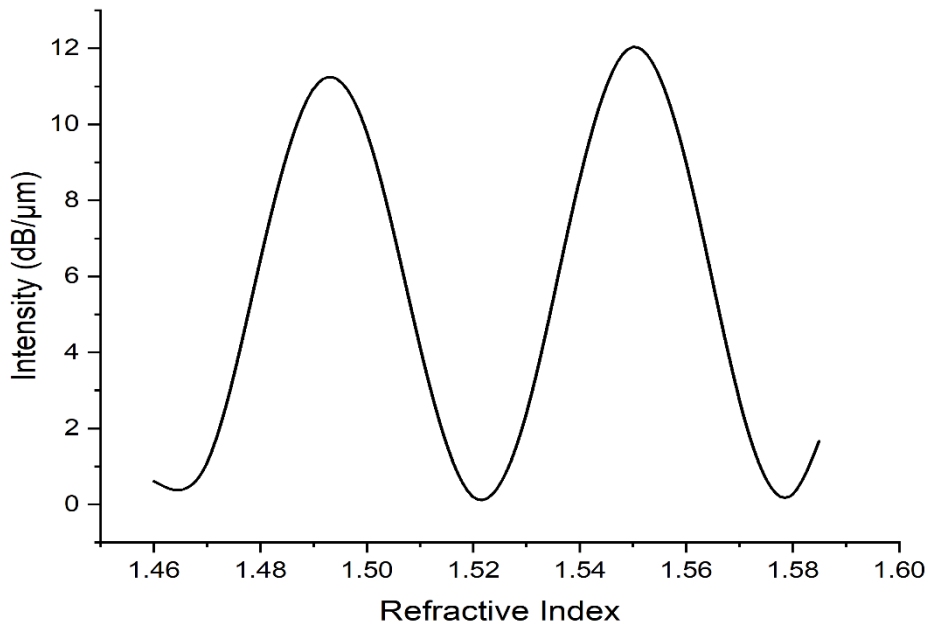
Figure 9.3: Intensity Interrogation Spectrum at 0.89 μm

The Intensity Interrogation was performed at 0.89 μm initially at Refractive Index range of 1.46-1.58. Constructive interferences are the points where the output intensity is the maximum, whereas the destructive interferences are where intensity tends to zero. It is observed that there is a series of constructive and destructive interferences with the change in analyte refractive index. With the change in RI, the propagation constant of the outer SPP mode changes whereas the inner SPP's propagation constant remains fairly the same. Hence, the phase difference between the two modes is a function of the provided analyte [73]. This primarily verifies that the proffered sensor model is sensitive to changes in RI and the wavelength interrogation can performed afterwards.

9.3.2 Wavelength Interrogation

Wavelength interrogation involves the change in wavelength for a particular analyte refractive index. This approach is better than Intensity interrogation method as it is more convenient in determining the interference points. The following figure portrays the total sensor response for analyte RIs of 1.47 and 1.48 using the wavelength interrogation approach.
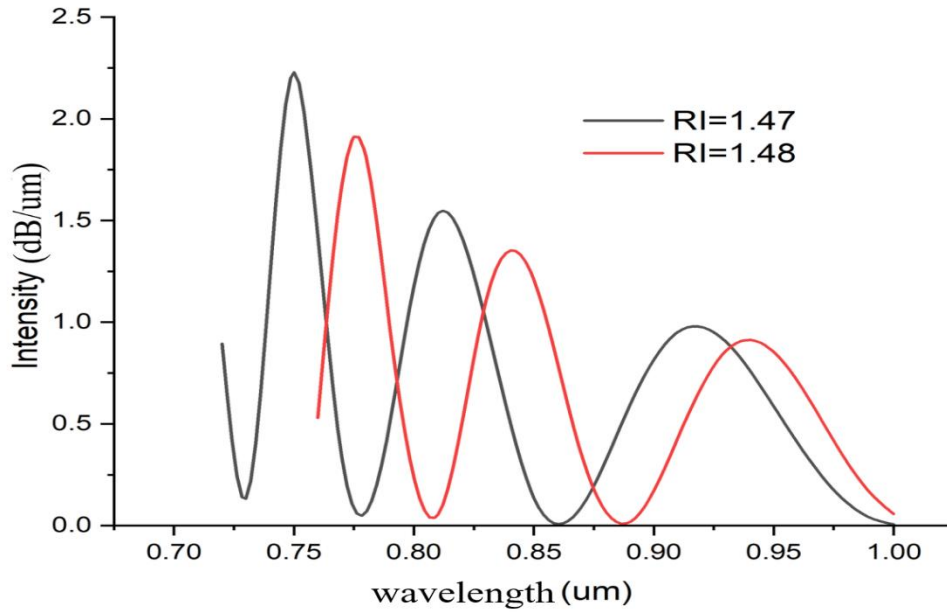
Figure 9.3: Total interference response for RI of 1.47 and 1.48

It is observable that, there are three peak interference peaks along the spectra. The constructive interference peak gradually decreases with the increase in wavelength for a particular RI. Moreover, the peak interference magnitude exhibits decreasing trend with the increase in analyte RI.

In our analysis, we have found out that the first interference peak of RI 1.44 shows the greatest magnitude and correspondingly the maximum sensitivity is at 1.44 RI. Taking into consideration of the advantage of the wavelength interrogation, we have performed our optimization technique for different structural parameters only for the first peak of 1.44 and 1.45 RIs.

It should be noted that, RI lower than 1.44 has been excluded as the outer SPP mode ceases to exist at low refractive indices.

9.3.3 Sensor Length Optimization

Sensor length plays the most impact in the alteration of the intensity of the two SPP modes and correspondingly, the most significant factor for sensitivity enhancement. Furthermore, sensor length does not give that much shift in the interference wavelength, so it

is the primary choice for structural optimization. Figure 9.5 depicts the interference spectra for variations in sensor length values.
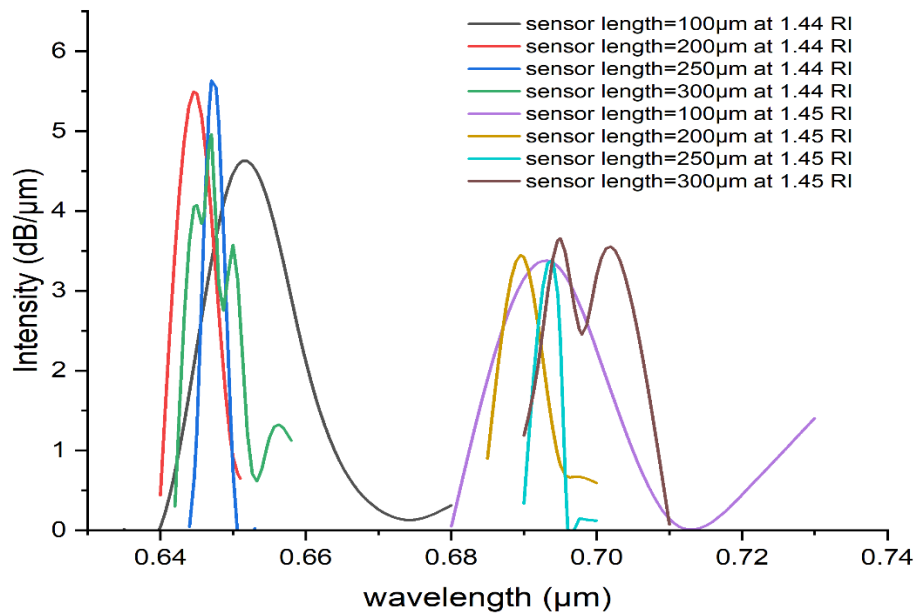
Figure 9.4: Interference pattern for varying sensor length

Initially, a sensor length (l_{pcf}) of 100µm is chosen and then increased to 300 µm. As seen from the graph, the maximum peak intensity value is obtained at 250 µm, after which the maximum peak value begins to decrease. More importantly, at 300 µm, a peak cluster is observed at a proximate wavelength. The sensitivity enhanced from 5.379 dB/RIU to 10.659 dB/RIU by increasing l_{pcf} from 100 µm to 250 µm. Hence, 250 µm is taken as the optimized sensor length.

9.3.4 Gold Layer Optimization

The thickness of the gold layer (t_g) has a slightly smaller impact in the change in intensity of the two SPP modes with the added alteration in the interference wavelength. The value of t_g was at first taken 0.30 µm. Next, t_g was increased by an increment of 0.1µm, up to 0.5µm. The figure in the following displays the different interference spectra due to change in gold layer thickness.
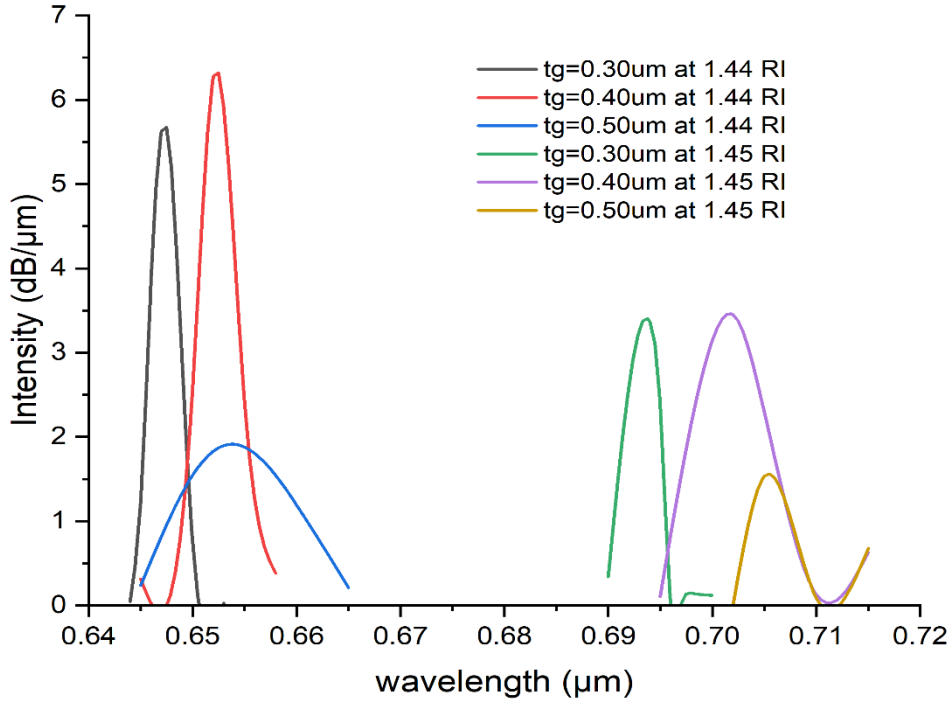
Figure 9.5: Interference spectra for varying gold layer thickness

As we can witness from the figure above, increasing the gold layer exhibits a red shift of the peak interference wavelength. On the otherhand, the peak intensity increases when t_g is enlarged from 0.30µm to 0.40 µm, but it drastically falls at 0.50 µm. Due to the combined effect of increased interference wavelength and difference in peak intensity, the sensitivity boosted from 10.659 dB/RIU to 14.152 dB/RIU. So the optimized gold layer thickness is 0.40 µm.

9.3.5 Doped Silica Layer Optimization

The doped silica layer does not play a major role in sensitivity enhancement. But to obtain the maximum sensor performance, its thickness has to be brought to the optimum value. Figure 9.7 shows the variation of the interference peak when the thickness of doped silica layer (t_s) was decreased from initial value of 0.40 um to 0.35 um.
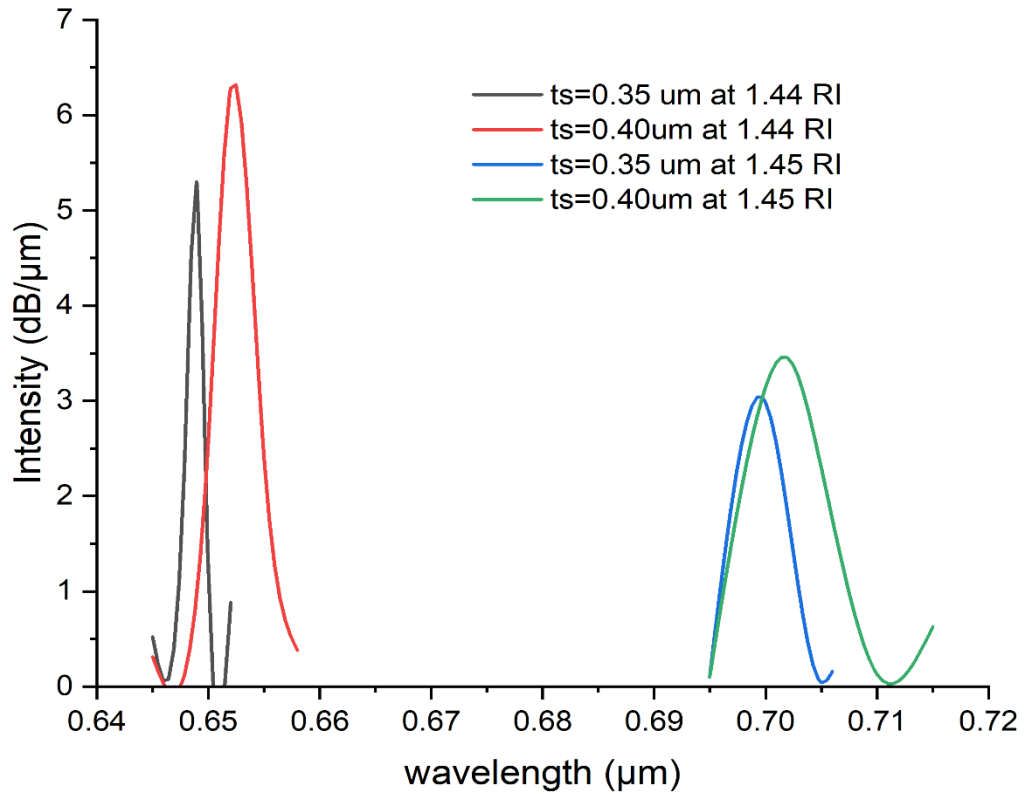
Figure 9.6: Interference spectra for variation in doped silica layer

With the decrease in t_s, there is a decrement in the difference between the peak interference magnitudes between the two RIs for respective thickness. But the difference in the interference wavelengths remains the same for both values of t_s. Hence, a fall in sensitivity (14.152 dB/RIU to 11.664 dB/RIU) is observed when t_s is decreased from 0.40 um to 0.35 um.

It should be noted that, enlargement in doped silica layer causes extinguish of the inner SPP mode. Hence, analysis for t_s greater than 0.40 um has been disregarded and 0.40 um is kept as the optimum thickness.

Apart from sensitivity, other performance parameters have been evaluated for the proposed MZI sensor model.

The crest interference angle is defined the angle that the sides of the interference peak makes, up to the point where the sides maintain linearity. For such sharp peaks, the intensity corresponding to the full-width half maxima is the desired length. The smaller the crest interference angle, more distinct is the peak and hence better responsiveness of the sensor.

After optimization of structural dimensions, the smallest crest interference angle obtained is 8.8˚.

Furthermore, the proposed sensor model obtained a quality factor of 102.5 along with 280 figure of merit and sensor resolution of 0.01.

9.4 Conclusion

A simple SMF-PCF-SMF Mach Zehnder Interferometer has been proposed, which has a high sensing range of 1.44-1.52. Very few PCF based sensors have the capability to detect analyte at such high refractive index. Various structural parameters have been optimized to obtain the best sensitivity. Other than sensitivity, quality factor, figure of merit and sensor resolution have also been evaluated. The sensor evinced a very high maximum sensitivity of 14.152 dB/RIU, along with 102.5 quality factor, 280 figure of merit and sensor resolution of 0.01. Due to the wide sensing range accompanied excellent sensitivity, we are confident that the proposed sensor model will play vital role in different analyte sensing applications.

Chapter 10

Future Prospects and Conclusion

10.1 Conclusion

In our thesis work, we have explored and implemented three different sensing mechanisms in photonic crystal fibers. Working on these designs, we have obtained extensive knowledge of PCF based sensors and have acknowledged the vast proficiency of PCFs and new ways of sensing could also be applied in the future. In our research work, we have mathematically modelled the required materials and developed the designs in COMSOL Multiphysics. The structural dimensions have been optimized to gain the best possible results from respective designs. Finally, we like to conclude by saying that through our thesis work, we have aided in the evolution of photonic crystal fiber based sensing and we are confident that it will inspire new researchers to work in the vast field of photonics and plasmonics.

10.2 Future Prospects

1. To use materials other than silica in the core of the PCF MZI sensor.

2. To explore sensors performance with different plasmonic materials.

3. Analyze the PCF MZI sensor with different air hole shapes, like elliptical, square and rectangular etc.

4. Implement other intricate PCF structures like, D-shaped, slotted etc.

5. To explore the proficiency of PCF bases sensors in measuring other physical parameters.

References

[1]   J. Homola, "Surface Plasmon Resonance Sensors for Detection of Chemical and Biological Species," *Chem. Rev.*, vol. 108, no. 2, pp. 462–493, Feb. 2008, doi: 10.1021/cr068107d.

[2]   J. Homola, "Present and future of surface plasmon resonance biosensors.," *Anal. Bioanal. Chem.*, vol. 377, no. 3, pp. 528–539, Oct. 2003, doi: 10.1007/s00216-003-2101-0.

[3]   B. D. Gupta and R. K. Verma, "Surface Plasmon Resonance-Based Fiber Optic Sensors: Principle, Probe Designs, and Some Applications," *J. Sensors*, vol. 2009, p. 979761, 2009, doi: 10.1155/2009/979761.

[4]   R. Otupiri, E. K. Akowuah, S. Haxha, H. Ademgil, F. AbdelMalek, and A. Aggoun, "A Novel Birefrigent Photonic Crystal Fiber Surface Plasmon Resonance Biosensor," *IEEE Photonics J.*, vol. 6, no. 4, pp. 1–11, 2014, doi: 10.1109/JPHOT.2014.2335716.

[5]   J. G. Ortega-Mendoza, A. Padilla-Vivanco, C. Toxqui-Quitl, P. Zaca-Morán, D. Villegas-Hernández, and F. Chávez, "Optical fiber sensor based on localized surface plasmon resonance using silver nanoparticles photodeposited on the optical fiber end," *Sensors (Basel).*, vol. 14, no. 10, pp. 18701–18710, Oct. 2014, doi: 10.3390/s141018701.

[6]   E. Akowuah, T. Gorman, H. Ademgil, S. Haxha, G. Robinson, and J. Oliver, "Numerical Analysis of a Photonic Crystal Fiber for Biosensing Applications," *Quantum Electron. IEEE J.*, vol. 48, pp. 1403–1410, Nov. 2012, doi: 10.1109/JQE.2012.2213803.

[7]   A. A. Rifat *et al.*, "Photonic crystal fiber based plasmonic sensors," *Sensors Actuators B Chem.*, vol. 243, pp. 311–325, 2017, doi: https://doi.org/10.1016/j.snb.2016.11.113.

[8]   B. Liedberg, C. Nylander, and I. Lunström, "Surface plasmon resonance for gas detection and biosensing," *Sensors and Actuators*, vol. 4, pp. 299–304, 1983, doi: https://doi.org/10.1016/0250-6874(83)85036-7.

[9]   M. A. Mollah, S. M. R. Islam, M. Yousufali, L. F. Abdulrazak, M. B. Hossain, and I. S. Amiri, "Plasmonic temperature sensor using D-shaped photonic crystal fiber," *Results Phys.*, vol. 16, p. 102966, 2020, doi: https://doi.org/10.1016/j.rinp.2020.102966.

[10]   B. Han *et al.*, "Simultaneous measurement of temperature and strain based on dual SPR effect in PCF," *Opt. Laser Technol.*, vol. 113, pp. 46–51, May 2019, doi: 10.1016/j.optlastec.2018.12.010.

[11] S. A. Maier, "Plasmonics: The Promise of Highly Integrated Optical Devices," *IEEE J. Sel. Top. Quantum Electron.*, vol. 12, pp. 1671–1677, 2006.

[12] S. P. Burgos, H. W. Lee, E. Feigenbaum, R. M. Briggs, and H. A. Atwater, "Synthesis and Characterization of Plasmonic Resonant Guided Wave Networks," *Nano Lett.*, vol. 14, no. 6, pp. 3284–3292, Jun. 2014, doi: 10.1021/nl500694c.

[13] A. Khaleque, M. A. R. Franco, and H. T. Hatorri, "Ultra-broadband and compact polarization splitter for sensing applications," in *Photonics and Fiber Technology 2016 (ACOFT, BGPP, NP)*, 2016, p. JM6A.2, [Online]. Available: http://opg.optica.org/abstract.cfm?URI=NP-2016-JM6A.2.

[14] W. Qin, S. Li, Y. Yao, X. Xin, and J. Xue, "Analyte-filled core self-calibration microstructured optical fiber based plasmonic sensor for detecting high refractive index aqueous analyte," *Opt. Lasers Eng.*, vol. 58, pp. 1–8, Jul. 2014, doi: 10.1016/j.optlaseng.2014.01.003.

[15] M. S. Islam, M. R. Islam, J. Sultana, A. Dinovitser, B. W.-H. Ng, and D. Abbott, "Exposed-core localized surface plasmon resonance biosensor," *J. Opt. Soc. Am. B*, vol. 36, no. 8, pp. 2306–2311, 2019, doi: 10.1364/JOSAB.36.002306.

[16] M. M. Rahman, F. Mou, M. Bhuiyan, and M. Islam, "Photonic crystal fiber based terahertz sensor for cholesterol detection in human blood and liquid foodstuffs," *Sens. Bio-Sensing Res.*, p. 100356, Jun. 2020, doi: 10.1016/j.sbsr.2020.100356.

[17] F. A. Mou, M. M. Rahman, M. R. Islam, and M. I. H. Bhuiyan, "Development of a photonic crystal fiber for THz wave guidance and environmental pollutants detection," *Sens. Bio-Sensing Res.*, vol. 29, p. 100346, Aug. 2020, doi: 10.1016/j.sbsr.2020.100346.

[18] M. Islam, M. Kabir, T. Khandoker, and M. Islam, "A novel hollow core terahertz refractometric sensor," *Sens. Bio-Sensing Res.*, vol. 25, p. 100295, Jul. 2019, doi: 10.1016/j.sbsr.2019.100295.

[19] J. Sultana, M. S. Islam, K. Ahmed, A. Dinovitser, B. W.-H. Ng, and D. Abbott, "Terahertz detection of alcohol using a photonic crystal fiber sensor," *Appl. Opt.*, vol. 57, no. 10, pp. 2426–2433, 2018, doi: 10.1364/AO.57.002426.

[20] M. S. Islam *et al.*, "A novel Zeonex based photonic sensor for alcohol detection in beverages," in *2017 IEEE International Conference on Telecommunications and Photonics (ICTP)*, 2017, pp. 114–118, doi: 10.1109/ICTP.2017.8285905.

[21] M. Islam, M. Hossain, S. Ali, J. Sultana, and M. Islam, "Design and Characterization of an Ultra Low Loss, Dispersion-Flattened Slotted Photonic Crystal Fiber for Terahertz Application," *J. Opt. Commun.*, Nov. 2018, doi: 10.1515/joc-2018-0152.

[22] A. Aming, M. Uthman, R. Chitaree, W. Mohammed, and B. M. A. Rahman, "Design and Characterization of Porous Core Polarization Maintaining Photonic Crystal Fiber for THz Guidance," *J. Light. Technol.*, vol. 34, no. 23, pp. 5583–5590, 2016, [Online]. Available: http://opg.optica.org/jlt/abstract.cfm?URI=jlt-34-23-5583.

[23] K. Nielsen, H. K. Rasmussen, A. J. L. Adam, P. C. M. Planken, O. Bang, and P. U. Jepsen, "Bendable, low-loss Topas fibers for the terahertz frequency range," *Opt. Express*, vol. 17, no. 10, pp. 8592–8601, 2009, doi: 10.1364/OE.17.008592.

[24] M. Ibadul Islam *et al.*, "Design of single mode spiral photonic crystal fiber for gas sensing applications," *Sens. Bio-Sensing Res.*, vol. 13, pp. 55–62, 2017, doi: https://doi.org/10.1016/j.sbsr.2017.03.001.

[25] H. Bao, K. Nielsen, H. K. Rasmussen, P. U. Jepsen, and O. Bang, "Fabrication and characterization of porous-core honeycomb bandgap THz fibers," *Opt. Express*, vol. 20, no. 28, pp. 29507–29517, 2012, doi: 10.1364/OE.20.029507.

[26] M. Rabiul Hasan, M. Ariful Islam, M. S. Anower, and S. M. A. Razzak, "Low-loss and bend-insensitive terahertz fiber using a rhombic-shaped core," *Appl. Opt.*, vol. 55, no. 30, pp. 8441–8447, 2016, doi: 10.1364/AO.55.008441.

[27] J. Noda, K. Okamoto, and Y. Sasaki, "Polarization-maintaining fibers and their applications," *J. Light. Technol.*, vol. 4, no. 8, pp. 1071–1089, 1986, doi: 10.1109/JLT.1986.1074847.

[28] J. C. Knight, T. A. Birks, P. S. J. Russell, and D. M. Atkin, "All-silica single-mode optical fiber with photonic crystal cladding," *Opt. Lett.*, vol. 21, no. 19, pp. 1547–1549, 1996, doi: 10.1364/OL.21.001547.

[29] J. C. Knight, J. Broeng, T. A. Birks, and P. S. J. Russell, "Photonic band gap guidance in optical fibers.," *Science*, vol. 282, no. 5393, pp. 1476–1478, Nov. 1998, doi: 10.1126/science.282.5393.1476.

[30] S. Chowdhury *et al.*, "Porous shaped photonic crystal fiber with strong confinement field in sensing applications: Design and analysis," *Sens. Bio-Sensing Res.*, vol. 13, pp. 63–69, 2017, doi: https://doi.org/10.1016/j.sbsr.2017.03.002.

[31] M. S. Habib, M. S. Habib, S. M. Razzak, Y. Namihira, M. A. Hossain, and A. Khan, "Broadband Dispersion Compensation of Conventional Single Mode Fibers Using Microstructure Optical Fiber," *Opt. - Int. J. Light Electron Opt.*, vol. 124, pp. 3851–3855, Oct. 2013, doi: 10.1016/j.ijleo.2012.12.014.

[32] R. W. Clough and E. L. Wilson, "EARLY FINITE ELEMENT RESEARCH AT BERKELEY 1," 1999.

[33]   F. L. Teixeira, "Time-Domain Finite-Difference and Finite-Element Methods for Maxwell Equations in Complex Media," *IEEE Trans. Antennas Propag.*, vol. 56, no. 8, pp. 2150–2166, 2008, doi: 10.1109/TAP.2008.926767.

[34]   J.-Y. Wu and R. Lee, "The advantages of triangular and tetrahedral edge elements for electromagnetic modeling with the finite-element method," *IEEE Trans. Antennas Propag.*, vol. 45, pp. 1431–1437, 1997.

[35]   E. Kretschmann and H. Raether, "Notizen: Radiative Decay of Non Radiative Surface Plasmons Excited by Light," *Zeitschrift für Naturforsch. A*, vol. 23, pp. 2135–2136, 1968.

[36]   A. Otto, "Excitation of nonradiative surface plasma waves in silver by the method of frustrated total reflection," *Zeitschrift für Phys. A Hadron. Nucl.*, vol. 216, no. 4, pp. 398–410, 1968, doi: 10.1007/BF01391532.

[37]   I. Pockrand, J. D. Swalen, J. G. I. I. Gordon, and M. R. Philpott, "Surface plasmon spectroscopy of organic monolayer assemblies," *Surf. Sci.*, vol. 74, no. 1, pp. 237–244, 1978, [Online]. Available: http://inis.iaea.org/search/search.aspx?orig_q=RN:09402862.

[38]   B. Liedberg, I. Lundström, and E. Stenberg, "Principles of biosensing with an extended coupling matrix and surface plasmon resonance," *Sensors and Actuators B-chemical*, vol. 11, pp. 63–72, 1993.

[39]   C. Striebel, A. Brecht, and G. Gauglitz, "Characterization of biomembranes by spectral ellipsometry, surface plasmon resonance and interferometry with regard to biosensor application," *Biosens. Bioelectron.*, vol. 9, no. 2, pp. 139–146, 1994, doi: https://doi.org/10.1016/0956-5663(94)80105-3.

[40]   S. Löfås and B. Johnsson, "A novel hydrogel matrix on gold surfaces in surface plasmon resonance sensors for fast and efficient covalent immobilization of ligands," *J. Chem. Soc.{,} Chem. Commun.*, no. 21, pp. 1526–1528, 1990, doi: 10.1039/C39900001526.

[41]   S. Sjölander and C. Urbaniczky, "Integrated fluid handling system for biomolecular interaction analysis.," *Anal. Chem.*, vol. 63, no. 20, pp. 2338–2345, Oct. 1991, doi: 10.1021/ac00020a025.

[42]   B. Gupta and A. Sharma, "Sensitivity evaluation of a multi-layered surface plasmon resonance-based fiber optic sensor: A theoretical study," *Sensors Actuators B Chem.*, vol. 107, pp. 40–46, May 2005, doi: 10.1016/j.snb.2004.08.030.

[43]   E. Descrovi, V. Paeder, L. Vaccaro, and H.-P. Herzig, "A virtual optical probe based on localized Surface Plasmon Polaritons," *Opt. Express*, vol. 13, no. 18, pp. 7017–7027,

2005, doi: 10.1364/OPEX.13.007017.

[44] C. R. Taitt, G. P. Anderson, and F. S. Ligler, "Evanescent wave fluorescence biosensors.," *Biosens. Bioelectron.*, vol. 20, no. 12, pp. 2470–2487, Jun. 2005, doi: 10.1016/j.bios.2004.10.026.

[45] M. Hautakorpi, M. Mattinen, and H. Ludvigsen, "Surface-plasmon-resonance sensor based on three-hole microstructured optical fiber," *Opt. Express*, vol. 16, no. 12, pp. 8427–8432, 2008, doi: 10.1364/OE.16.008427.

[46] T. Ahmed, A. K. Paul, M. S. Anower, and S. M. A. Razzak, "Surface plasmon resonance biosensor based on hexagonal lattice dual-core photonic crystal fiber," *Appl. Opt.*, vol. 58, no. 31, pp. 8416–8422, 2019, doi: 10.1364/AO.58.008416.

[47] F. Haider, R. A. Aoni, R. Ahmed, M. S. Islam, and A. E. Miroshnichenko, "Propagation Controlled Photonic Crystal Fiber-Based Plasmonic Sensor via Scaled-Down Approach," *IEEE Sens. J.*, vol. 19, no. 3, pp. 962–969, 2019, doi: 10.1109/JSEN.2018.2880161.

[48] R. Kashyap and G. Nemova, "Surface Plasmon Resonance-Based Fiber and Planar Waveguide Sensors," *J. Sensors*, vol. 2009, p. 645162, 2009, doi: 10.1155/2009/645162.

[49] M. R. Momota and M. R. Hasan, "Hollow-core silver coated photonic crystal fiber plasmonic sensor," *Opt. Mater. (Amst).*, vol. 76, pp. 287–294, Feb. 2018, doi: 10.1016/j.optmat.2017.12.049.

[50] C. Caucheteur, T. Guo, and J. Albert, "Review of plasmonic fiber optic biochemical sensors: improving the limit of detection.," *Anal. Bioanal. Chem.*, vol. 407, no. 14, pp. 3883–3897, May 2015, doi: 10.1007/s00216-014-8411-6.

[51] Y. Liu *et al.*, "High-sensitivity plasmonic temperature sensor based on gold-coated D-shaped photonic crystal fiber," *Appl. Opt.*, vol. 58, no. 18, pp. 5115–5121, 2019, doi: 10.1364/AO.58.005115.

[52] M. S. Islam *et al.*, "Dual-polarized highly sensitive plasmonic sensor in the visible to near-IR spectrum," *Opt. Express*, vol. 26, no. 23, pp. 30347–30361, 2018, doi: 10.1364/OE.26.030347.

[53] H. Liang, T. Shen, Y. Feng, H. Liu, and W. Han, "A D-Shaped Photonic Crystal Fiber Refractive Index Sensor Coated with Graphene and Zinc Oxide," *Sensors*, vol. 21, no. 1, 2021, doi: 10.3390/s21010071.

[54] A. A. Rifat, G. A. Mahdiraji, Y. G. Shee, M. J. Shawon, and F. R. M. Adikan, "A Novel Photonic Crystal Fiber Biosensor Using Surface Plasmon Resonance," *Procedia Eng.*, vol. 140, pp. 1–7, 2016, doi: https://doi.org/10.1016/j.proeng.2015.08.1107.

[55] J. Lou, T. Cheng, S.-G. Li, and X. Zhang, "Surface plasmon resonance photonic crystal fiber biosensor based on gold-graphene layers," *Opt. Fiber Technol.*, vol. 50, pp. 206–211, Jul. 2019, doi: 10.1016/j.yofte.2019.03.028.

[56] M. Islam *et al.*, "A Hi-Bi Ultra-Sensitive Surface Plasmon Resonance Fiber Sensor," *IEEE Access*, vol. 7, pp. 79085–79094, Jun. 2019, doi: 10.1109/ACCESS.2019.2922663.

[57] J. N. Dash and R. Jha, "SPR Biosensor Based on Polymer PCF Coated With Conducting Metal Oxide," *IEEE Photonics Technol. Lett.*, vol. 26, no. 6, pp. 595–598, 2014, doi: 10.1109/LPT.2014.2301153.

[58] B. K. Paul *et al.*, "The design and analysis of a dual-diamond-ring PCF-based sensor," *J. Comput. Electron.*, vol. 19, Sep. 2020, doi: 10.1007/s10825-020-01509-2.

[59] A. A. Rifat *et al.*, "Surface Plasmon Resonance Photonic Crystal Fiber Biosensor: A Practical Sensing Approach," *IEEE Photonics Technol. Lett.*, vol. 27, no. 15, pp. 1628–1631, 2015, doi: 10.1109/LPT.2015.2432812.

[60] I. Yakasai, P. E. Abas, S. Ali, and F. Begum, "Modelling and simulation of a porous core photonic crystal fibre for terahertz wave propagation," *Opt. Quantum Electron.*, vol. 51, p. 122, Apr. 2019, doi: 10.1007/s11082-019-1832-x.

[61] J. R. DeVore, "Refractive Indices of Rutile and Sphalerite," *J. Opt. Soc. Am.*, vol. 41, no. 6, pp. 416–419, 1951, doi: 10.1364/JOSA.41.000416.

[62] P. Bing, S. Huang, J. Sui, H. Wang, and Z. Wang, "Analysis and Improvement of a Dual-Core Photonic Crystal Fiber Sensor," *Sensors*, vol. 18, no. 7, 2018, doi: 10.3390/s18072051.

[63] M. Islam, J. Sultana, R. A. Aoni, A. Dinovitser, B. Ng, and D. Abbott, "Terahertz Sensing in a Hollow Core Photonic Crystal Fiber," *IEEE Sens. J.*, vol. 18, pp. 4073–4080, May 2018, doi: 10.1109/JSEN.2018.2819165.

[64] M. Ahasan Habib, M. Shamim Anower, and M. Rabiul Hasan, "Highly birefringent and low effective material loss microstructure fiber for THz wave guidance," *Opt. Commun.*, vol. 423, pp. 140–144, 2018, doi: https://doi.org/10.1016/j.optcom.2018.04.022.

[65] M. Islam *et al.*, "Zeonex based asymmetrical terahertz photonic crystal fiber for multichannel communication and polarization maintaining applications," *Appl. Opt.*, vol. 57, pp. 666–672, Feb. 2018, doi: 10.1364/AO.57.000666.

[66] I. K. Yakasai, A. Rahman, P. E. Abas, and F. Begum, "Theoretical Assessment of a Porous Core Photonic Crystal Fiber for Terahertz Wave Propagation," *J. Opt. Commun.*, vol. 43, no. 2, pp. 199–209, 2022, doi: doi:10.1515/joc-2018-0206.

[67] G. Woyessa, A. Fasano, C. Markos, A. Stefani, H. Rasmussen, and O. Bang, "Zeonex microstructured polymer optical fiber: fabrication friendly fibers for high temperature and humidity insensitive Bragg grating sensing," *Opt. Mater. Express*, vol. 7, p. 286, Jan. 2017, doi: 10.1364/OME.7.000286.

[68] I. Yakasai, P. E. Abas, S. F. Kaijage, W. Caesarendra, and F. Begum, "Proposal for a Quad-Elliptical Photonic Crystal Fiber for Terahertz Wave Guidance and Sensing Chemical Warfare Liquids," *Photonics* , vol. 6, no. 3. 2019, doi: 10.3390/photonics6030078.

[69] Y. Wang, C. R. Liao, and D. N. Wang, "Femtosecond laser-assisted selective infiltration of microstructured optical fibers," *Opt. Express*, vol. 18, no. 17, pp. 18056–18060, 2010, doi: 10.1364/OE.18.018056.

[70] M. Rakibul Islam, M. M. I. Khan, F. Mehjabin, J. Alam Chowdhury, and M. Islam, "Design of a fabrication friendly & highly sensitive surface plasmon resonance-based photonic crystal fiber biosensor," *Results Phys.*, vol. 19, p. 103501, 2020, doi: https://doi.org/10.1016/j.rinp.2020.103501.

[71] M. Islam *et al.*, "Design and Analysis of a Biochemical Sensor Based on Surface Plasmon Resonance with Ultra-high Sensitivity," *Plasmonics*, Jan. 2021, doi: 10.1007/s11468-020-01355-9.

[72] Y. Ming, Z. Wu, H. Wu, F. Xu, and Y. Lu, "Surface Plasmon Interferometer Based on Wedge Metal Waveguide and Its Sensing Applications," *IEEE Photonics J.*, vol. 4, pp. 291–299, Feb. 2012, doi: 10.1109/jphot.2012.2186562.

[73] S. Mirzanejhad, A. Ghadi, and M. Daraei, "Numerical study of nanoscale biosensor based on surface plasmon polariton propagation in Mach-Zehnder interferometer structure," *Phys. B Condens. Matter*, vol. 557, Dec. 2018, doi: 10.1016/j.physb.2018.12.038.